MODELING AND NUMERICAL SIMULATION OF DROPLET SPREADING AND SOLIDIFICATION AFTER IMPACT ON A SOLID SUBSTRATE

by

Samuel B. Johnson

A thesis submitted to the Faculty and Board of Trustees of the Colorado School of Mines in partial fulfillment of the requirements for the degree of Master of Science (Engineering Systems).

Golden, Colorado
Date 11/12/2001

Signed: ____________________
Samuel B. Johnson

Approved: ____________________
Dr. Jean-Pierre Delplanque
Thesis Advisor

Golden, Colorado
Date: 11/14/01

____
Dr. Joan Gosink
Professor and Head,
Division of Engineering

ABSTRACT

Spray deposition processes are an efficient method for the production of net-shape products. During spray deposition processes the final material properties and quality depend significantly on the phenomena involved in the spreading and solidification of individual droplets impacting the target substrate. It is therefore necessary to build a thorough understanding of the phenomena involved in individual droplet impacts to understand the overall spray deposition process. The focus of the present study is the development of analytical and numerical tools for the prediction of droplet spreading and solidification after impact on a solid substrate. Simple analytical models, while generally less accurate than numerical simulation, typically provide physical insight more readily than numerical simulation. Furthermore, when control and optimization strategies are sought, numerical simulation is too computationally intensive, and analytical models are required. However, due to greater accuracy and detail, numerical simulation may be used to evaluate, and make improvements to analytical models. First, a thermal energy solver, using a finite volume/difference approximation, is developed and incorporated into an existing Navier-Stokes solver for interfacial flows (RIPPLE). This thermal energy solver is based on an enthalpy formulation of the thermal energy conservation equation, which is preferred to a temperature formulation, because it does not require explicit tracking of the solid front. The numerical procedure is detailed, and verification and validation cases are presented. Next, an analytical model for droplet impacts is developed using an integral method. The model includes the influences of the impact angle, thermal contact resistance and rapid solidification. Finally, results from numerical simulations, the analytical model, and available experimental data are compared.

TABLE OF CONTENTS

LIST OF FIGURES

LIST OF TABLES

ACKNOWLEDGEMENTS

I gratefully acknowledge the financial support of the United States Department of Energy, Idaho Operations Office (DE-FC07-00ID 13816), The Brown Foundation, and the Center for Combustion and Environmental Research. I would like to thank Dr. Mark Lusk and Dr. Robert Kee for contributing their time to serve on my thesis committee, and finally, I would like to express my sincere thanks Dr. Jean-Pierre Delplanque, my advisor, for his guidance and patience during my research.

CHAPTER 1

INTRODUCTION AND BACKGROUND

Currently, ingot metallurgical (I/M) processing is the most widely used method for the production of aluminum strip, accounting for 70% of domestic production. However, I/M processing is capital and energy intensive, because of the need to eliminate casting flaws through hot working.

Twin-roll casting is an alternative method for the production of aluminum strip, often viewed as offering the greatest potential in the production of aluminum strip. Twin-roll casting combines solidification and hot rolling into a single step by feeding liquid metal between water-cooled mill rolls. However, twin-roll casting is not widely used because of the technical hurdles that must be overcome: improving microstructural quality, process reliability, and production rate. Furthermore, alloy choices in twin-roll casting are limited.

Spray deposition offers many potential benefits to the production of aluminum strip, both in terms of cost, and improved material properties. Cost reductions result from process simplification, the elimination of hot rolling, and homogenization-unit operators, and improved energy efficiency. In terms of material properties, spray deposition offers improved metallurgical homogeneity with equiaxed grain structures, and reduced levels of segregation due to rapid solidification. Furthermore, spray deposition may be used for the development of highly alloyed aluminum for high-temperature and high-strength applications, and the production of aluminum alloys with increased formability. Also, spray deposition has the potential to accept higher contaminant levels, increasing recyclability. Technical hurdles to the commercial viability of spray deposition for the production of aluminum strip include reduction of porosity at the deposit substrate interface and uniformity of the strip profile.

Spray rolling is a promising technology currently being developed for the production of aluminum strip. Spray rolling involves atomization of molten aluminum, quenching droplets in-flight to a semi-solid state, deposition onto consolidation rolls, and rolling the deposited material into a strip while still in a highly formable state. Spray rolling offers the benefits found in traditional spray deposition processes combined with the elimination of porosity at the deposit substrate interface, and a uniform strip profile. Furthermore, it has recently been shown that spray rolling allows the production of aluminum alloys that can not be twin-roll cast due to constraits on the solidification temperature range.

The successful development and commercialization of the spray-rolling process requires a thorough understanding of the various physical mechanisms that influence the final material quality. The overall spray-rolling process involves phenomena with vastly different length and time scales. It is, therefore, impractical to model the process as a whole; rather, the process is broken down into distinct sub-processes and modeled in a piecewise fashion, with the eventual goal of model integration, and overall process characterization. The spray-rolling process can be divided into several stages: melt atomization, in-flight quenching of droplets, droplet deposition, and consolidation rolling.

The focus of the present study is the development of numerical and theoretical tools to predict the spreading and solidification of a droplet impacting a solid substrate, with application to the deposition of droplets during the spray-rolling process. Numerical simulation gives a great deal of detail and accuracy in the study of droplet impacts. However, because numerical simulation is computationally intensive, it does not lend itself well to process control and optimization. Furthermore, the influence of individual physical mechanisms may be concealed by the complexity of the analysis. Through a simplified perspective, simple analytical models readily offer insight into the individual physical mechanisms influencing droplet spreading and solidification, and are not hindered by excessive computational time. An accurate analytical model is therefore desired for the study of droplet impacts, with the higher accuracy and detail found in numerical simulation used as a tool to evaluate and improve the analytical model.

In order to simulate droplet impacts, an algorithm capable of modeling interfacial flows must be used. Two approaches are taken for the simulation of interfacial flows: Lagrangian deforming grid methods; and Eulerian fixed grid methods. In Lagrangian deforming grid methods the mesh deforms with the motion of the fluid, and tracking of the free surface is accomplished by merely locating one of the mesh lines on the free surface [1]. However, Lagrangian methods are computationally intensive, and do not lend themselves well to large fluid deformations, due to the frequent remeshing required. In Eulerian fixed grid methods, an interface tracking, or reconstruction procedure is required. The location of the interface may be either tracked by markers placed on the interface [2], or reconstructed from a scalar function. In level set methods the scalar function corresponds to the distance from the free surface [3, 4], while in the volume of fluid method, the free surface is reconstructed from a scalar function describing the fractional volume of fluid [5, 6, 7].

Waldvogel and Poulikakos [8] have extensively studied the spreading and solidification of droplets in solder jetting, a process to dispense small solder droplets for the mounting of micro-electronic components. During this process, inertial effects are small, and droplets undergo relatively little deformation. Consequently Waldvogel and Poulikakos were able to apply a Lagrangian deforming grid approach to the problem. However, during spray deposition processes, droplets undergo severe deformation, and the Lagrangian approach is not practical.

A more suitable approach to the simulation of droplet impact problems is the volume of fluid (VOF) method. The VOF method accepts large fluid deformation and calculates coalescence and breakup seamlessly. The VOF method is used extensively in the simulation of droplet impacts. Delplanque and Rangel [9], and later Zhang [10] used the VOF method to model droplet spreading and solidification. In both cases, solidification was modeled using the Neumann solution to the Stefan solidification problem. Pasandideh-Fard *et al.* [11] also used VOF method, but included an energy solver to model solidification, in a study on the spreading and solidification of tin droplets on a steel plate. The implementations of the VOF method discussed above are for two-dimensional modeling of droplet impacts; however, Bussmann *et al.* [12] have also extended the VOF method to three-dimensions, allowing for inclusion of three-dimensional aspects of droplet impact: splashing, angled impact, and impact on irregular surfaces. However, solidification was not included in the three dimensional model. A three-dimensional VOF code including solidification, TRUCHAS, is currently under development at Los Alamos National Laboratory.

In the present study, an energy solver is added to an existing Navier-Stokes solver for incompressible free surface flows, RIPPLE (developed a Los Alamos National Laboratory [7, 13]). The energy solver is based on an enthalpy formulation of the thermal energy conservation equation, preferred, because it does not require explicit tracking of the solid front, and the effect of solidification on the flow field is modeled using an artificial drag force [14]. This modified version of RIPPLE will allow validation and evaluation of an analytical droplet impact model, discussed below.

Simple analytical models tend to be less realistic in their assumptions than numerical simulation; however, they readily allow investigation of individual physical mechanisms, which influence droplet spreading and solidification. This facilitates a greater understanding of the relative importance of these physical mechanisms. Furthermore, because of their computational efficiency, analytical models are well suited for process control, and optimization, major necessities in the development and commercialization of spray deposition processes. Many algebraic and differential droplet impact models have been developed based on a mechanical energy balance. Healy *et al.* [15] reviewed several of these models and found that they typically over predict the maximum droplet spread by roughly 45%. Among the models reviewed by Healy *et al.* was an integral model proposed by Madejski [16].

Madejski [16] devised an integral model for predicting the spreading and solidification of a molten droplet after impacting a solid substrate. He used a mechanical energy balance to describe droplet deformation:

$$\frac{d}{dt'}\left(E_k + E_p + E_d\right) = 0, \tag{1.1}$$

where E_k is the kinetic energy of the droplet, E_p is the potential energy associated with surface tension, and E_d is the mechanical energy lost through viscous dissipation. For Madejski's integral model, the shape and velocity field of the spreading droplet were prescribed. The droplet is assumed to take the shape of a cylindrical disk after it comes in contact with the substrate, and a simple velocity field was chosen with the requirement that it satisfy the continuity equation and the no-slip condition at the solid front:

$$\omega_x = -2C'x^2, \;\; \omega_r = C'xr, \tag{1.2}$$

where ω_x, and ω_r are the axial and radial velocity components, respectively, b is the uniform liquid thickness, and C' is a time dependent quantity. To model solidification of the spreading droplet, Madejski used the Neumann solution to the Stefan solidification problem [17], which is strictly valid for one-dimensional solidification with the solid front at the equilibrium melting temperature, and does not account for thermal contact resistance at the substrate surface. Madejski's integral model was an inventive approach to the droplet impact problem, and provides the basis for many droplet impact models that followed. However, there were some shortcomings in his analysis.

The velocity field used by Madejski [16] was chosen with the only requirements being that is satisfy the continuity equation and the no-slip condition. Markworth and Saunders [18] recognized that a further requirement for the prescribed velocity field should be to satisfy the no-shear condition at the free surface. With this additional requirement they devised an improved velocity field:

$$\omega_x = 2C'\left(\frac{x^3}{3} - bx^2\right), \quad \omega_r = C'r\left(2xb - x^2\right). \tag{1.3}$$

Evaluation of Madejski's velocity field showed that mechanical energy was effectively being transmitted to the splat at its free surface, because the no-shear condition was not satisfied.

Furthermore, the derivation of the viscous dissipation term in Madejski's mechanical energy balance was incorrect [16]. Madejski gave the rate of viscous dissipation to be

$$\frac{dE_d}{dt'} = \int_0^R 2\pi\tau\bar{\omega}_r r\,dr. \tag{1.4}$$

where dE_d/dt' is the rate of viscous dissipation, $\bar{\omega}$ is the radial velocity averaged over the thickness of the spreading droplet, and

$$\tau = \mu\frac{\partial\omega_r}{\partial x}. \tag{1.5}$$

Delplanque and Rangel [19] presented an accurate derivation of the viscous dissipation term, which is

$$\frac{dE_D}{dt'} = \int_V \mu\Phi dV, \tag{1.6}$$

where V indicates integration over the volume of the spreading droplet, and for Madejski's velocity field, and the improved velocity field

$$\Phi = \frac{\bar{\bar{\tau}} : \nabla \boldsymbol{\omega}}{\mu} = 2\left(\frac{\partial \omega_r}{\partial r}\right)^2 + 2\frac{\omega_r^2}{r^2} + 2\left(\frac{\partial \omega_x}{\partial x}\right)^2 + \left(\frac{\partial \omega_r}{\partial x}\right)^2, \tag{1.7}$$

where $\bar{\bar{\tau}}$ is the viscous stress tensor.

Delplanque and Rangel [19] performed a detailed comparison of Madejski's model [16] and an improved model incorporating Markworth and Saunders' improved velocity field [18], and the accurate derivation of the viscous dissipation term. They found that the errors in Madejski's model contributed to a over estimate of droplet spreading, and that the discrepancy became even more pronounced as the influence of viscous dissipation increased.

There are also physical phenomena that significantly influence droplet spreading and solidification, which were not accounted for in Madejski's model [16]. First, the previously discussed models assume that the droplet is impinging normally to the substrate. However, droplet impacts are rarely normal to the target substrate. Also, during droplet impacts, the droplet-substrate interfacial energy may have a significant influence on droplet spreading, and it is unlikely that there will be perfect thermal contact between the droplet and substrate. Finally, because of the high cooling rates found in spray deposition processes, droplets may undergo significant undercooling.

The models discussed above are concerned with droplets impinging normally to the target substrate; however, in real spray processes, droplet impacts are rarely normal. This may be due to dispersion in the spray cone, or due to a moving substrate, which is important in the spray rolling process. The influence of the impact angle on droplet spreading has been studied extensively by Sobolev and Guilemany [20] using an integral model similar to that discussed above. However, many problems arise in the analysis presented by Sobolev and Guilemany. First, despite claims to the contrary, the velocity field they impose on the spreading droplet does not satisfy the continuity equation. Furthermore, the velocity field is given an exponential time dependence with no physical explanation or connection to mechanical energy conservation. The assumptions and errors made by Sobolev and Guilemany undermine the reliability of their results, and their work will be discussed no further.

While the prescribed shape of the splat in the previously discussed models limits the contact angle to 90^o, actual contact angles may be very different form 90^o, and significantly effect droplet spreading. Therefore, the interfacial energy should not be limited by the imposed droplet shape. Zhang [10] adopted the improvements made by Delplanque and Rangel [19] and modified the potential energy term of the mechanical energy balance to include an equilibrium contact angle, which may be different from 90^o. However, during droplet impacts, the contact angle may deviate significantly from its equilibrium value. Advancing contact angles are larger than the equilibrium contact angle, and may vary significantly during droplet spreading. Zhang did not include the dynamic effects of the contact angle in his analysis.

The Neumann solution to the Stefan solidification problem [17], used extensively in droplet impact models, assumes perfect thermal contact between the droplet and substrate. A thermal contact resistance typically exists between the droplet and substrate, which is an important factor in droplet cooling and solidification [21]. This resistance is the result of surface roughness, surface impurities and gas entrapment. While thermal contact resistance plays a significant role in droplet spreading, it is not a well-quantified parameter. Wang and Matthys [21] studied the thermal contact resistance for molten copper droplets impacting various metallic substrates by matching model calculations with experimental data. They found that the thermal contact resistance might vary by several orders of magnitude during the solidification of a droplet. Because thermal contact resistance is so poorly quantified, it can, at best, be seen as a fitting parameter in analytical models.

Due to high cooling rates, droplets may also undergo significant undercooling. The influence of undercooling has been studied extensively for the quenching of droplets in-flight [22], and for surface melting [23], but has not been given enough attention with respect to droplet spreading and solidification on a solid substrate. Wang and Matthys [24] presented a numerical technique for rapid solidification using a control volume integral approach, with applications to splat cooling, but did not include this analysis is the modeling of droplet impact dynamics. The effects of undercooling and thermal contact resistance where included in a droplet impact model presented by Chung and Rangel [25]. They adopted the improved model used by Delplanque and Rangel [19] and included a numerical approximation to the thermal energy conservation equation to determine solid growth. While the assumptions used are more realistic than those accompanying the Neumann solution to the Stefan solidification problem [17], the complexity of the model is significantly increased, reducing the benefits obtained through simplicity in analytical models.

In the present study, an analytical model is developed to predict the spreading and solidification of droplets. This model, based on the improvements made by Delplanque and Rangel [19], includes the influence of the droplet impact angle, and presents improvements to the solidification model. The solidification model has been adapted to include thermal contact resistance, and the influence of rapid solidification. The influence of the impact angle, thermal contact resistance, and rapid solidification are then studied. Finally, a brief comparison is made between the analytical model, the numerical model, and available experimental results [26].

CHAPTER 2

NUMERICAL SIMULATION OF DROPLET IMPACTS

Numerical simulation provides a valuable tool in the analysis of droplet impacts. While it is computationally intensive, and not suitable for process control or optimization, numerical simulation offers a great deal of detail and accuracy with regard to the dynamics of droplet spreading and solidification.

The simulation of droplet impacts requires calculation of the velocity field within the droplet as well as the ability to accurately locate the free surface of the droplet. In Lagrangian deforming grid methods the grid moves and deforms with the motion of the fluid, and no further models are required to locate the free surface. However, breakup and coalescence phenomena are difficult to model. The Lagrangian method is also very computationally intensive, due to the frequent remeshing required with large grid deformations. Waldvogel and Poulikakos [8] developed a code using the Lagrangian deforming grid method to simulate droplet impacts. They have applied the code to the study of low-inertia droplet impacts typical of the solder jetting process. This process is well suited to their code, because the droplets undergo relatively little deformation. However, this is a special case; droplets in most manufacturing applications undergo severe deformations for which the Lagrangian approach would not be well suited.

Eulerian fixed grid methods are better suited to the droplet impact problem. In Eulerian fixed grid methods, the location of the free surface must be tracked or reconstructed. In particular, the volume of fluid (VOF) method uses a scalar function, F, the fractional volume of fluid, to locate the free surface. The VOF method is well suited to the droplet impact problem because it accommodates large fluid deformations very easily, and incorporates breakup and coalescence seamlessly. The VOF method has been extensively used to simulate droplet impacts [9, 10, 11, 12].

To accurately simulate the droplet impacts, the influence of solidification on the flow field must be evaluated. Efforts to simulate the solidification and spreading processes of droplet impacts have been presented in literature, and different approaches have been taken with regards to solidification. Rather than evaluating heat transfer within the droplet, Delplanque and Rangel [9], and later Zhang [10] used a locally one-dimensional solidification model, based on the Neumann solution to the Stefan solidification problem [17], to evaluate solid growth. Waldvogel and Poulikakos [8] used the temperature formulation of the thermal energy conservation equation, requiring the application of a heat balance at the solid-liquid interface, and explicit tracking of the solid front. Finally, Pasandideh-Fard *et al.* used an enthalpy formulation of the thermal energy conservation equation. From a numerical perspective, the enthalpy formulation is very attractive, because it does not require explicit tracking of the solid front.

The work discussed herein is dedicated to including an energy solver into an existing Navier-Stokes solver for free surface flows (RIPPLE) in order to allow detailed evaluation of droplet impact, spreading, and solidification. An enthalpy formulation of the thermal energy conservation equation is used, and a numerical approach is taken, which is consistent with the existing flow solver. The numerical procedure is detailed, and several test cases are presented.

2.1 Analysis

To accurately describe droplet spreading and solidification, both the flow field and the thermal state of the droplet must be know. To this end, the thermal energy conservation equation must be evaluated, in addition to momentum conservation and continuity.

2.1.1 Governing Equations

The fluid flow aspect of the droplet impact problem is solved using RIPPLE [7]. This code is suited for two-dimensional and axisymmetric flow with surface tension acting on free surfaces. Fluid flow within the droplet is governed by the incompressible continuity equation

$$\nabla \cdot \mathbf{V} = 0, \tag{2.1}$$

where $\vec{V}$ is the velocity of the fluid, and the transport of fluid momentum,

$$\frac{\partial \mathbf{V}}{\partial t} + \nabla \cdot (\mathbf{V}\mathbf{V}) = -\frac{1}{\rho}\nabla p + \frac{1}{\rho}\nabla \cdot \tau + \mathbf{g} + \frac{1}{\rho}\mathbf{F}_b - K\mathbf{V}, \tag{2.2}$$

where p is the pressure, $\mathbf{g}$ is gravitational acceleration, $\mathbf{F}_b$ is a volumetric body force used to model surface tension, and $-K\mathbf{V}$ is an artificial drag force used to model the effect of solidification on the flow field.

Heat transfer in the droplet is governed by an enthalpy formulation of the thermal energy conservation equation. The viscous dissipation term has been neglected giving

$$\frac{\partial h}{\partial t} + \nabla \cdot (hF\mathbf{V}) = -\nabla \cdot \mathbf{q}, \tag{2.3}$$

where h is the volumetric specific enthalpy. The heat flux, $\mathbf{q}$ is given by Fourier's law:

$$\mathbf{q} = -k\nabla T, \tag{2.4}$$

where k is the thermal conductivity and T is the temperature.

To model droplet impacts, the location of the free surface must be determined. RIPPLE uses a VOF method to locate and reconstruct the free surface. The VOF method uses a scalar function F, the fractional volume of the fluid, to locate the free surface. The transport equation for F is

$$\frac{\partial F}{\partial t} + \nabla \cdot (F\mathbf{V}) = 0, \tag{2.5}$$

where $F = 0$ in the void, $F = 1$ in the fluid, and $0 < F < 1$ at the free surface.

RIPPLE uses a continuum surface force (CSF) model to calculate surface tension at the free surface. The CSF model treats surface tension as a local volumetric body force acting at the free surface:

$$\mathbf{F}_s = \sigma\kappa\nabla F, \tag{2.6}$$

where σ is the surface tension, assumed constant, and κ is the curvature of the surface. The effects of surface tension on the flow field can then be modeled by including the volumetric body force in the momentum transport equation (Equation 2.2):

$$\mathbf{F}_b = \mathbf{F}_s. \tag{2.7}$$

The effect of solidification on the flow field is modeled using an artificial drag force ($-K\mathbf{V}$) [14], where the drag coefficient, K, is related to the enthalpy

$$K = \begin{cases} 0 & h > h_\ell \\ K_{max}\left(h - h_\ell\right) / \left(h_s - h_\ell\right) & h_\ell < h < h_s \\ \infty & h < h_\ell \end{cases}, \tag{2.8}$$

where h_ℓ is the liquidus enthalpy and h_s is the solidus enthalpy.

2.1.2 Numerical Procedure

In RIPPLE [7], a two-step projection method is used to approximate the continuity and momentum equations. This method has been expanded to three steps to accommodate the artificial drag force. The first step calculates the incremental change in the velocity field due to viscous effects, gravitational acceleration, and surface tension,

$$\frac{\tilde{\mathbf{V}} - \mathbf{V}^n}{\delta t} = -\nabla \cdot (\mathbf{V}\mathbf{V})^n + \frac{1}{\rho^n}\nabla \cdot \tau^n + \mathbf{g}^n + \frac{1}{\rho^n}\mathbf{F}_b^n. \tag{2.9}$$

The second step applies the artificial drag force used to model solidification,

$$\tilde{\mathbf{V}}' = \tilde{\mathbf{V}} e^{-K\delta t}. \tag{2.10}$$

Finally, the third step, combining the incompressibility condition and the pressure term, projects the solution onto a zero-divergence velocity field,

$$\nabla \cdot \left[\frac{1}{\rho^n}\nabla p^{n+1}\right] = \frac{\nabla \cdot \tilde{\mathbf{V}}'}{\delta t}. \tag{2.11}$$

Excluding the addition of the artificial drag force, the solution of the momentum and continuity equations remain unchanged in the modified version of RIPPLE [7].

A two-step approximation, designed to be consistent with the method used for momentum and VOF transport in RIPPLE [7], is made to the thermal energy conservation equation. The first step computes the incremental change in the enthalpy due to conduction,

$$\frac{\tilde{h} - h^n}{\delta t} = -\nabla \cdot \mathbf{q}^n. \tag{2.12}$$

The second step approximates the incremental change in the enthalpy due to advection,

$$\frac{h^{n+1} - \tilde{h}}{\delta t} = -\nabla \cdot (hF\mathbf{V})\,. \tag{2.13}$$

Finally, because the divergence of the velocity field is not zero, but a small value dependent upon the convergence criteria, a divergence correction may need to be calculated.

The conduction and advection equations are calculated using a finite volume/difference approximation. Equation 2.12 is expressed numerically as

$$\begin{aligned} \tilde{h}_{i,j} = h^n_{i,j} \quad & -\frac{\delta t}{r^\delta_i \delta x_i}\left(r^\delta_{i+1/2,j} q^{\,n}_{xi+1/2,j} - r^\delta_{i-1/2} q^{\,n}_{xi-1/2,j}\right) \\ & -\frac{\delta t}{\delta y_j}\left(q^{\,n}_{yi,j+1/2} - q^{\,n}_{yi,j-1/2}\right), \end{aligned} \tag{2.14}$$

where the heat flux in the x-direction is computed

$$q^{\,n}_{xi+1/2,j} = \frac{T^n_{i+1,j} - T^n_{i,j}}{R^n_{i+1/2,j}}, \tag{2.15}$$

and

$$R^n_{i+1/2,j} = \frac{\delta x_i}{k^n_{i,j}} + \frac{\delta x_{i+1}}{k^n_{i+1,j}}. \tag{2.16}$$

The heat flux in the y-direction is computed similarly.

The conduction term is computed explicitly, and consequently, will be only conditionally stable. Furthermore, the stability criteria may be much lower than that required for momentum transport, necessitating the use of very small time steps. To avoid this problem, sub-cycling is implemented in the solution of the conduction term.

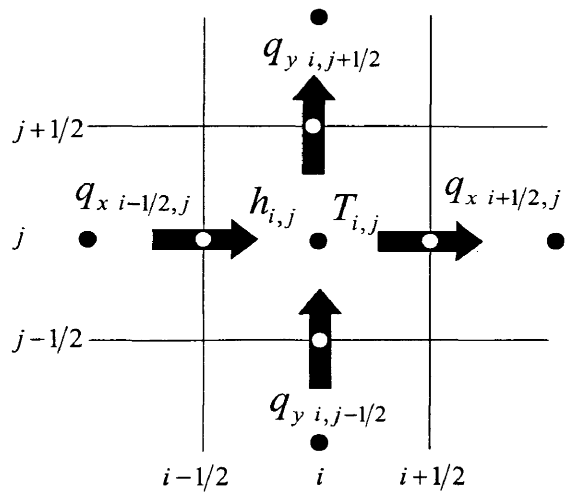

Figure 2.1: Cell heat flux schematic.

Equation 2.13 is discretized by integrating over the cell faces, giving

$$\begin{aligned} h_{i,j}^{n+1} = \tilde{h}_{i,j} \quad & -\frac{\delta t}{r_i^\delta \delta x_i}\left(r_{i+1/2}^\delta u_{i+1/2,j}^n \langle F\rangle_R \tilde{h}_R - r_{i-1/2} u_{i-1/2,j}^n \langle F\rangle_L \tilde{h}_L\right) \\ & -\frac{\delta t}{\delta y_j}\left(v_{i,j+1/2}^n \langle F\rangle_T \tilde{h}_T - v_{i,j-1/2}^n \langle F\rangle_B \tilde{h}_B\right) \end{aligned} \tag{2.17}$$

where r_i is the radial distance, and δ is zero in Cartesian coordinates, and unity in cylindrical coordinates. The quantity $< F >_R$ is the fraction of fluid on the right face in the upwind cell (similarly for the other faces), where the subscripts R, L, B, and T denote the right, left, bottom, and top faces, respectively.

2.2 Results and Discussion

Several test cases were run to verify various aspects of the numerical procedure and validate its application to droplet-impact problems. First, conduction is evaluated by comparison with an analytical solution for steady-state conduction in a unit square. Then, solidification is compared to the Neumann solution to the Stefan solidification problem, and enthalpy advection is included for finite-gap stagnation flow. Finally, results are compared to experimental data for droplet impacts in very different spreading regimes.

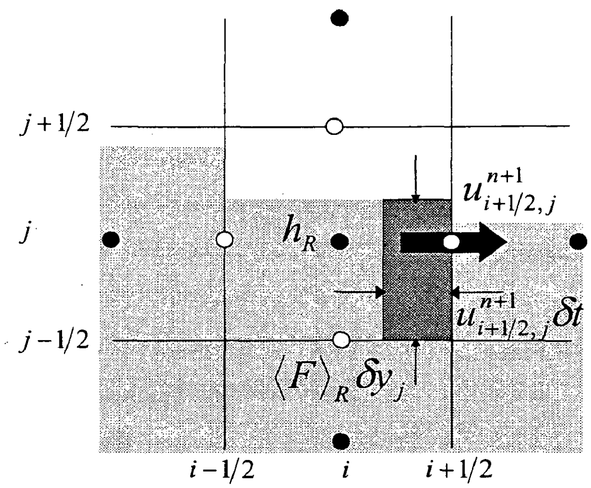

Figure 2.2: Enthalpy advection schematic.

2.2.1 Two-dimensional Steady-state Conduction

Consider steady-state conduction in a unit square subject to the boundary conditions

$$T(0,y) = T(1,y) = T(x,0) = 0, \quad T(x,1) = 1. \tag{2.18}$$

There exists an analytical solution, obtained through the method of separation of variables [27]. This series solution is expressed as

$$T(x,y) = \frac{2}{\pi} \sum_{n=1}^{\infty} \frac{(-1)^{n+1} + 1}{n} \sin(n\pi x) \frac{\sinh(n\pi y)}{\sinh(n\pi)}. \tag{2.19}$$

The analytical solution is compared with results from the modified version of RIPPLE. The numerical procedure used is for transient analysis; it was, therefore, necessary to allow the case to run for sufficient time ($t = 4s$) to reach a steady-state solution. In Figure 2.3, the steady-state analytical solution is compared to the temperature profile calculated at $4s$. It is seen that the results from the modified version of RIPPLE and the analytical solution (Equation 2.19).

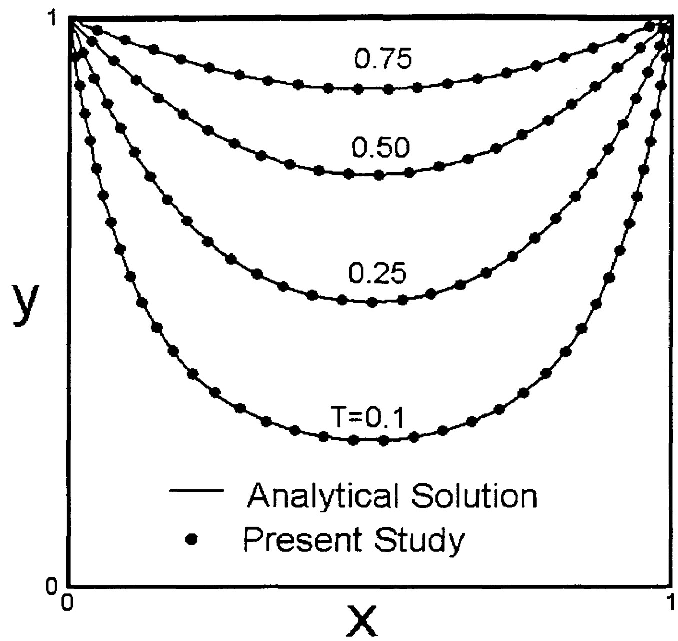

Figure 2.3: Numerical and analytical solutions to steady state-conduction in the unit square.

2.2.2 One-dimensional Solidification

Consider a semi-infinite medium initially liquid at the equilibrium melting temperature. The left boundary ($x = 0$) is suddenly brought to a temperature T_0, below the equilibrium melting temperature and solidification begins. The position of the solid-liquid interface is found to be proportional to the square root of time:

$$y(t) = 2\lambda \left(\alpha_s t\right)^{1/2}, \tag{2.20}$$

where α_s is the thermal diffusivity, and λ is a function of the Stefan number (see Appendix B).

The analytical solution to the solid front position is compared with results from the modified version of RIPPLE. The simulation was run for solidification of aluminum: $c_p = 1086$ J/kg − K, $k = 94.13$ W/m^{3}K, $\rho = 2357$ kg/m^3, $T_m = 933$ K, with a substrate temperature $T_0 = 298$ K. In Figure 2.4 the simulation results show very good agreement with the analytical solution.

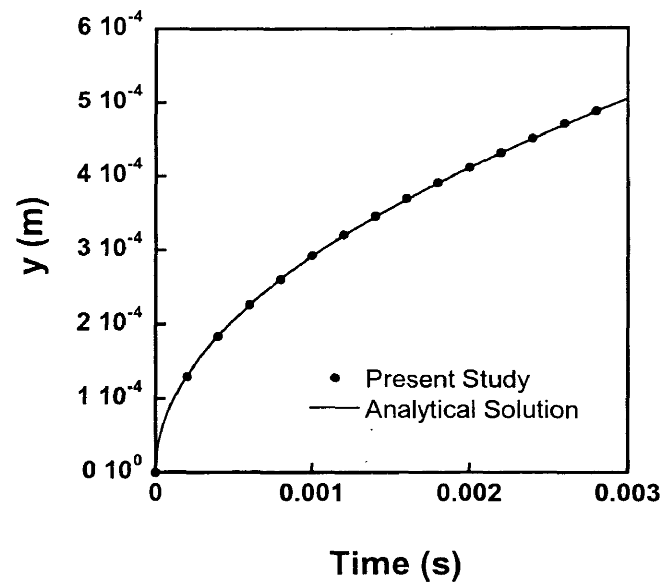

Figure 2.4: Numerical and analytical solutions to the Stefan solidification problem.

2.2.3 Finite-gap Stagnation Flow

Consider steady flow between a parallel manifold and plate of infinite extent, separated by a distance L, with a manifold inlet temperature T_{in} and velocity V, and a plate surface temperature T_s. For constant density and transport properties, flow and heat transfer will be governed by the finite-gap stagnation flow equations [28]:

$$\frac{d\hat{v}_z}{d\hat{z}} + 2\hat{V}_r = 0, \tag{2.21}$$

$$\hat{v}_z \frac{d\hat{V}_r}{d\hat{z}} + \hat{V}_r = \hat{\Lambda}_r + \frac{1}{\mathrm{Re}} \frac{d^2\hat{V}_r}{d\hat{z}^2}, \tag{2.22}$$

$$\hat{u} \frac{d\theta}{d\hat{z}} = \frac{1}{\mathrm{RePr}} \frac{d^2\theta}{d\hat{z}^2}. \tag{2.23}$$

where the dimensionless variables are $\theta = (T - T_{in}) / (T_s - T_{in})$, $\hat{v}_z = v_z/V$, and $\hat{V}_r = Lv_r/rV$.

Results from the modified version of RIPPLE where compared to a numerical solution of Equation 2.21, Equation 2.22, and Equation 2.23 (Figure 2.6). Again the simulation was run for sufficient time to reach a steady-state solution. The simulation

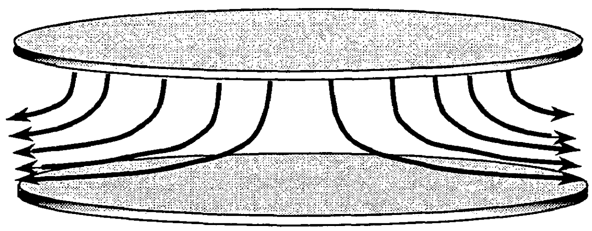

Figure 2.5: Stagnation flow schematic.

results from the modified version of RIPPLE were taken near the axis of symmetry to avoid any edge effects. The comparison shows a very good agreement between the results obtained from the modified version of RIPPLE and the numerical solution to Equation 2.21, Equation 2.22 and Equation 2.23.

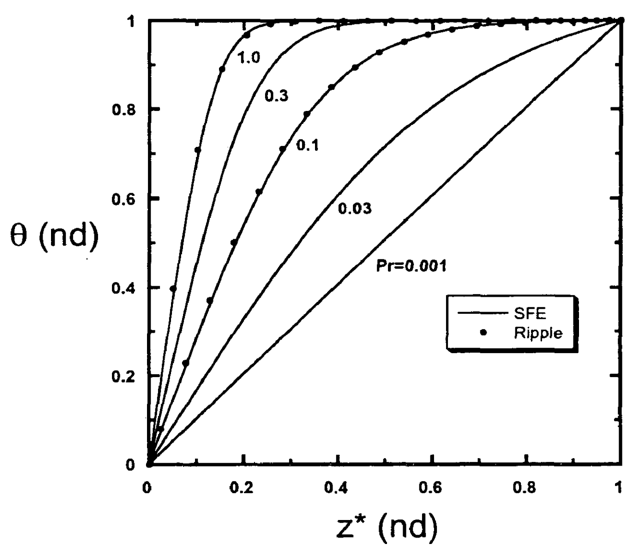

Figure 2.6: Comparison of solutions to steady-state finite-gap stagnation flow.

2.2.4 Low-inertia Droplet Impact

Solder jetting is process whereby small solder droplets are dispensed for the mounting of micro-electronic components. Solder jetting involves low inertia droplet impacts, which are dominated by surface tension effects. This process has been studied extensively by Waldvogel and Poulikakos [8] both experimentally and numerically.

Property	Value
Density	8218 $\mathrm{kg/m^3}$
Surface Tension	0.345 $\mathrm{N/m}$
Kinematic Viscosity	$3.2 \times 10^{-7}\ \mathrm{m^2/s}$
Latent Heat	$4.2 \times 10^4\ \mathrm{J/kg}$
Liquid Conductivity	25 $\mathrm{W/m-K}$
Solid Conductivity	48 $\mathrm{W/m-K}$
Liquid Specific Heat	238 $\mathrm{J/kg-K}$
Solid Specific Heat	176 $\mathrm{J/kg-K}$

Table 2.1: Physical properties of a eutectic lead-tin solder droplet.

A simulation was computed for a single molten solder droplet impacting a cold substrate and solidifying. The droplet spreads, and recoils repeatedly as it solidifies. This process leaves ripples on the final solidified solder bump. The modified version of RIPPLE was able to capture this phenomenon, as can be seen in Figure 2.7. Results from the modified version of RIPPLE agree well with experimental results obtained by Waldvogel and Poulikakos [8].

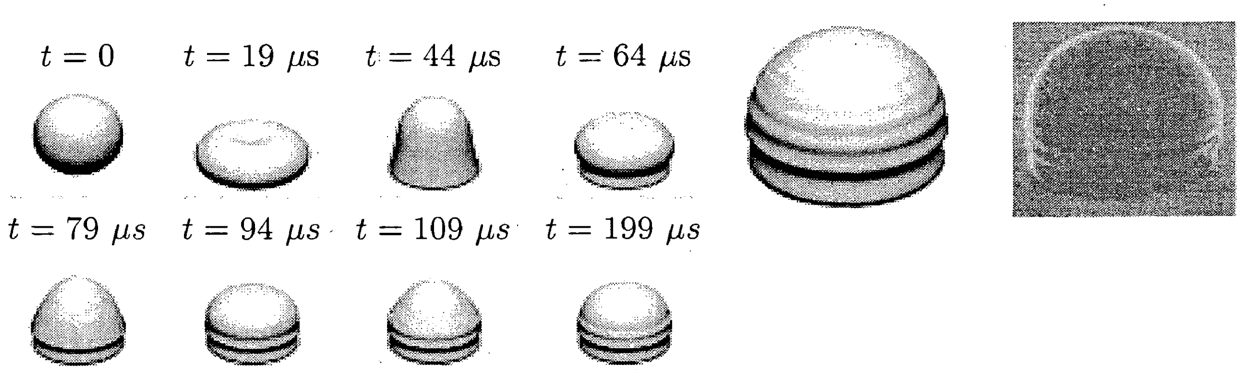

Figure 2.7: Simulation of a 50 μm solder droplet solidifying under conditions typical for solder jetting applications [8].

2.2.5 High-inertia Droplet Impact

Aziz *et al.* [26] have experimentally studied molten tin droplets impacting and solidifying on a stainless steel surface. Photographs were taken for 2.7mm tin droplet impacting at velocities between 1 and 4m/s, and substrate temperatures ranging from 298 to 513K. A simulation was run for the case of a 2.7mm tin droplet with a velocity of 2m/s, and a substrate temperature of 298K. The results from the modified version of RIPPLE were compared with the experimental results obtained by Aziz *et al.* (Figure 2.8). The simulation shows excellent agreement with the experimental results, even capturing the recoil of liquid from the edge of the droplet back over the solidified portion in the center.

Property	Value
Density	$7000\ \mathrm{kg/m^3}$
Surface Tension	$0.544\ \mathrm{N/m}$
Kinematic Viscosity	$2.6 \times 10^{-7}\ \mathrm{m^2/s}$
Latent Heat	$5.9 \times 10^{4}\ \mathrm{J/kg}$
Liquid Conductivity	$30\ \mathrm{W/m-K}$
Solid Conductivity	$66.6\ \mathrm{W/m-K}$
Liquid Specific Heat	$242\ \mathrm{J/kg-K}$
Solid Specific Heat	$227\ \mathrm{J/kg-K}$

Table 2.2: Physical properties of a tin droplet.

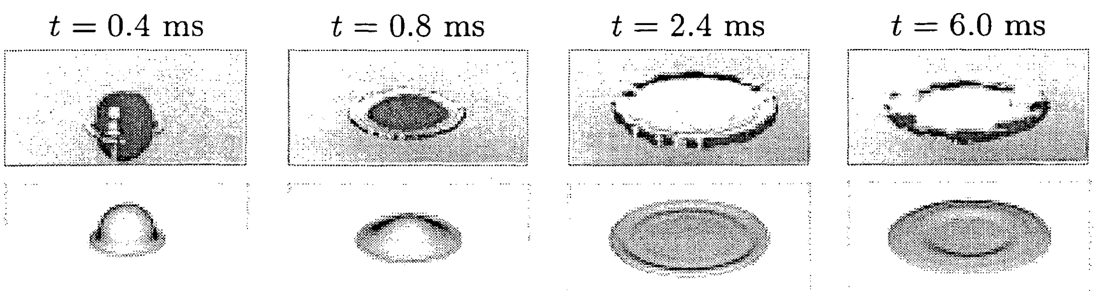

Figure 2.8: Spreading and solidification of a 2.7 mm tin droplet impacting a cold substrate at 2.0 m/s, Aziz *et al.* [26].

2.2.6 Discussion

An enthalpy-based thermal-energy solver has been implemented into an existing Navier-Stokes solver for incompressible free-surface flows (RIPPLE). Several test cases were successfully run including: steady-state conduction, one-dimensional solidification, finite-gap stagnation flow, and droplet impact cases in very different spreading regimes. The results in each case showed very good agreement with the corresponding analytical solution, or experimental observations.

The spreading dynamics seen in the high-inertia droplet impact case (Figure 2.8 are very different than those observed in the low-inertia droplet impact case(Figure 2.7). In the high-inertia case (Re = 2045, We = 139) droplet inertia plays a dominant role, resulting in a thin solidified splat, while in the low-inertia case (Re = 156, We = 1.2) surface tension dominates the spreading process. The results from both cases where in very good agreement, indicating a wide range of validity for the modified version of RIPPLE.

However, there are many phenomena, which influence droplet spreading and solidification that have not been included in the current analysis. Droplet impacts often involve three-dimensional phenomena, which can not be modeled with the two-dimensional code presented above. These phenomena include: angled droplet impacts, splashing, and impact on a non-uniform surface. There are also aspects of solidification, which have not been considered; droplets often undergo significant undercooling, due to high cooling rates. Furthermore, RIPPLE uses a very basic contact line model, which does not account for the dynamic aspects of contact line motion.

CHAPTER 3

MODELING OF DROPLET IMPACTS

Spray deposition is an efficient method to produce net and near-net shape products. However, spray deposition is not a mature technology. A major issue in the development of spray deposition processes is the development of adequate process control. This requires a thorough understanding of the various physical mechanisms involved, as well as their relative importance with respect to the characteristics of the final product. Simple analytical models, while generally less accurate than numerical simulation, typically provide physical insight more readily than numerical simulation. Furthermore, if the eventual goal is the development of a process control strategy, analytical models are necessary for their computational efficiency. During spray deposition processes, the final material quality depends significantly on the spreading and solidification of individual droplets impinging on a target substrate. Consequently, significant attention has been given to the development of analytical models for droplet spreading and solidification.

Madejski [16] presented an integral approach to the droplet impact problem. He derived an expression for the splat deformation, using a global mechanical energy balance, and assuming a cylindrical splat shape and axisymmetric velocity field, which satisfied the continuity condition, and the no-slip condition at the solid front. The Neumann solution to the Stefan solidification problem was used to evaluate solid growth. That model has since been improved; Markworth and Saunders [18] proposed an improved velocity field, which satisfied the no-shear condition at the free surface, as well as the continuity equation. Delplanque and Rangel [19] incorporated the improved velocity field and presented an accurate derivation of the viscous dissipation term, and Zhang [10] included the influence of contact adhesion. Many other droplet impact models have also been presented in the literature; however, relatively little attention has been given to the influence of the impact angle, thermal contact resistance or rapid solidification.

The models discussed above are concerned with a droplet impinging normally to the target substrate; however, droplet impacts are seldom normal to the target substrate in actual spray processes. Off-normal impacts may occur because of dispersion in the spay cone, or due to a moving substrate. Furthermore, There is experimental evidence that the impact angle may affect porosity distribution in the resulting material; Annavarapu *et al* [29] observed an increasing porosity in spray deposited materials away from the spray centerline, and at increasing substrate velocities (Figure 3.1).

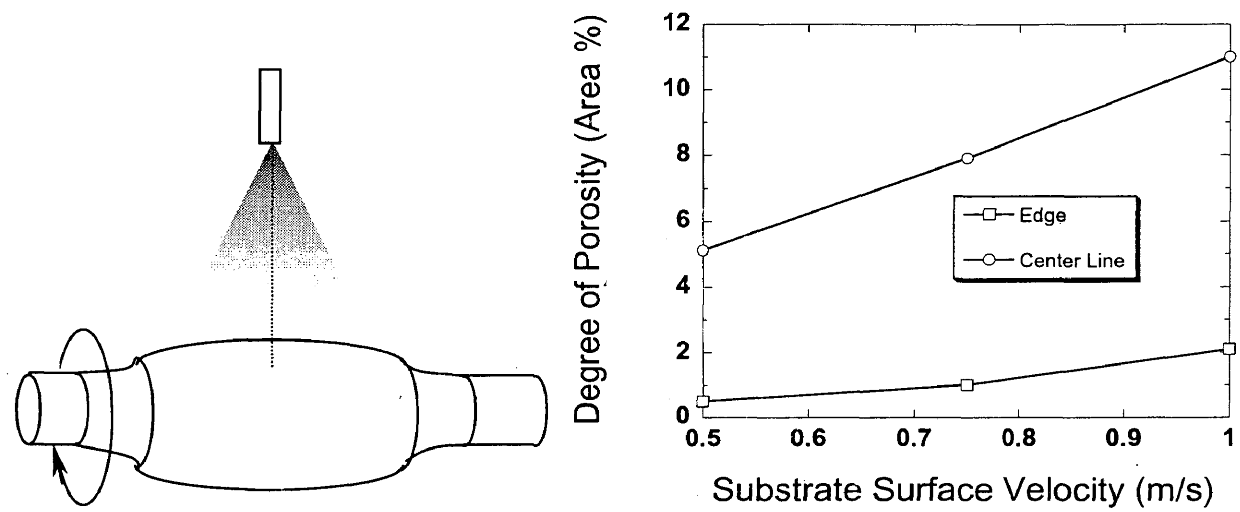

Figure 3.1: Porosity distribution in spray deposited material [29].

The analysis described herein expands upon the improved integral model proposed by Delplanque and Rangel [19] to include the effects of an off-normal impact. A three dimensional velocity field is adopted, which satisfies the no-shear condition at the free surface and the continuity equation. Furthermore, a non-axisymmetric shape is chosen for the resulting splat and a mechanical energy balance is used to descibe splat deformation.

The Neumann solution to the Stefan solidification problem assumes perfect contact between the droplet and substrate; however, a thermal contact resistance will typically exist between the splat and substrate. Furthermore, Wang and Matthys [30] found that thermal contact resistance may play a dominant roll in droplet spreading and solidification. This contact resistance is the result of gas entrapment that limits the actual area of contact, and is influenced by the substrate roughness and the substrate material. Wang and Matthys [21] studied the thermal contact resistance by fitting experimental data to a solidification model to determine the coefficient of heat transfer between the droplet and substrate. The present study uses a linear approximation to the solid thickness as a function of time to evaluate the effects of thermal contact resistance on droplet spreading and solidification.

Due to the high solidification rates present in spray deposition processes, solidification may be kinetically driven. Wang and Matthys presented a numerical technique for rapid solidification using a control-volume integral approach, with applications to splat cooling, but did not include their model in the analysis of droplet spreading dynamics. Chung and Rangel [25] have presented an original approach to the rapid solidification of a droplet, incorporating a numerical approximation to the thermal energy equation to evaluate the solid fraction in the model presented by Delplanque and Rangel [19]. The present study develops a simplified method for evaluating the solid growth in a spreading droplet, which is consistent with the level of accuracy of the splat deformation model and includes the effects of droplet undercooling. A global thermal energy balance and a linear law for the kinetic solid growth rate are used.

The analysis of an integral energy-conservation model for off-normal droplet impacts, and methods for determining the splat solid fraction are presented, with or without the influence of thermal contact resistance and undercooling. The analysis is followed by a study of the influence of the droplet impact angle and a comparison of solidification models.

3.1 Analysis

The configuration of interest for this study is that of a liquid droplet (diameter D) impinging on a flat solid substrate at an angle, γ, measured from the substrate normal, with a velocity, $\boldsymbol{\omega}$ (Figure 3.2). After impact, the droplet spreads and may solidify. An integral approach, based on a mechanical energy balance, is used to model this scenario. Consequently, a velocity field and splat shape are prescribed in a manner allowing for an accurate representation of an angled impact. Furthermore, solidification is modeled with or without the influences of thermal contact resistance and undercooling.

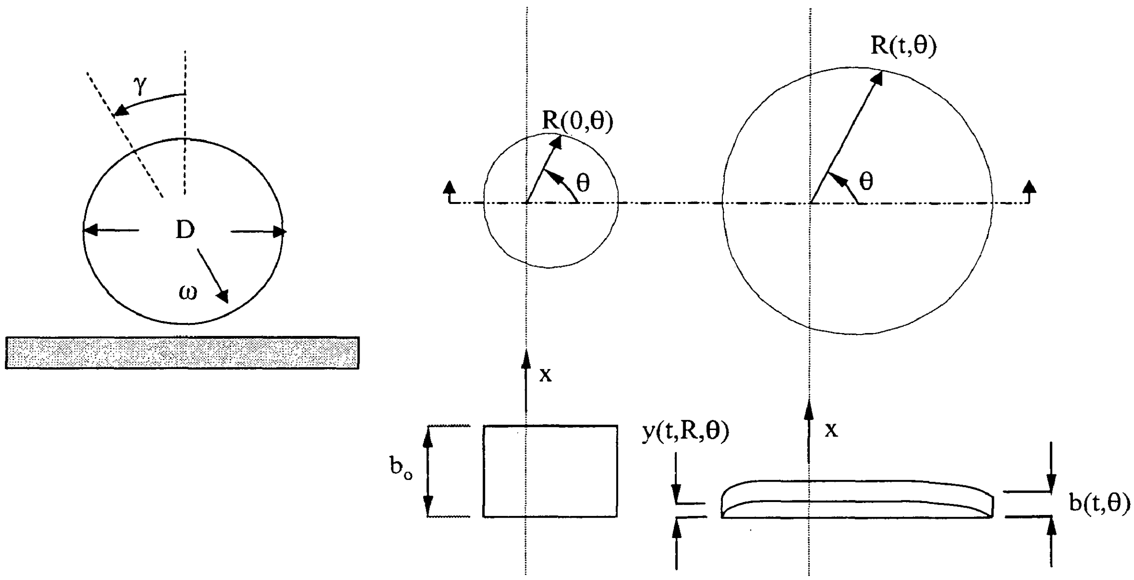

Figure 3.2: Problem schematic.

3.1.1 Mechanical Energy

A mechanical energy balance is used to describe the behavior of the deforming splat after impact [16]. The mechanical energy balance is given by

$$\frac{d}{dt'}\left(E_k + E_p + E_d\right) = 0, \tag{3.1}$$

where E_k is the kinetic energy, E_d is the mechanical energy lost through viscous dissipation, and E_p is the potential energy associated with surface tension. Delplanque and Rangel's [19] derivations of the kinetic, potential, and dissipative terms of the energy balance are expanded here to accommodate the three-dimensional velocity field and the non-axisymmetric shape of the splat.

The total kinetic energy is found by integrating over the volume of the splat. If x, r and θ are the axial, radial and circumferential coordinates, respectively, and ρ_ℓ

is the liquid density, the kinetic energy is defined

$$E_k = \int_0^{2\pi} \int_0^{R} \int_0^{b} \frac{1}{2} \rho_\ell \left(\omega_x^2 + \omega_r^2 + \omega_\theta^2 \right) dx dr d\theta, \tag{3.2}$$

where ω_x, ω_r, and ω_θ are the axial, radial and circumferential velocity components, respectively. The liquid thickness, b, is a function of time, and the splat radius, R, is a function of time and the circumferential coordinate (see §3.1.3).

The potential energy associated with surface tension is found to be proportional to the sum of the vertical and horizontal surface areas [19]. The potential energy associated with the splat-substrate interface is neglected in the present study. Consequently, the potential energy term can be expressed as

$$E_p = \sigma \left\{ \int_0^{2\pi} \int_0^{R} r dr d\theta + b \int_0^{2\pi} \left[R^2 + \left(\frac{\partial R}{\partial \theta} \right)^2 \right]^{1/2} d\theta \right\}, \tag{3.3}$$

where σ denotes the surface energy between the liquid and gas, the first integral in the Equation 3.3 is the horizontal portion of the surface area, and the second integral is the vertical portion.

In general terms, the rate of viscous dissipation is

$$\frac{dE_d}{dt'} = \int_V \mu \Phi dV = \int_0^{2\pi} \int_0^{R} \int_0^{b} \frac{\bar{\bar{\tau}} : \nabla \omega}{\mu} dx dr d\theta, \tag{3.4}$$

where μ is the viscosity and $\bar{\bar{\tau}}$ is the viscous stress tensor. For the three-dimensional velocity field used in the present model, Φ may be expressed in terms of the velocity components:

$$\begin{aligned} \Phi \; = \; & 2 \left\{ \left(\frac{\partial \omega_r}{\partial r} \right)^2 + \left[\frac{1}{r} \left(\frac{\partial \omega_\theta}{\partial \theta} + \omega_r \right) \right]^2 + \left(\frac{\partial \omega_x}{\partial x} \right)^2 \right\} \\ & + \left(\frac{\partial \omega_\theta}{\partial x} \right)^2 + \left(\frac{\partial \omega_r}{\partial x} \right)^2 + \left[\frac{1}{r} \left(\frac{\partial \omega_r}{\partial \theta} - \omega_\theta \right) + \frac{\partial \omega_\theta}{\partial r} \right]^2 . \end{aligned} \tag{3.5}$$

3.1.2 Three-dimensional Velocity Field

The mechanical energy balance presented above (Equation 3.1) can be solved using an integral method. This requires that the velocity field inside the splat be prescribed. Adequate representation of an off-normal droplet impact requires a three-dimensional velocity field; furthermore, the velocity field chosen for droplet impact problems should satisfy the no-shear condition at the free surface, the no-slip condition at the solid-liquid interface and the continuity equation. In addition to the above criteria, the velocity field chosen should be physically relevant to the droplet impact problem.

The velocity field used in the present study is the result of weighted superposition of the two-dimensional velocity field proposed by Markworth and Saunders [18], which accounts for the normal component of the droplet impact velocity, and a velocity field parallel to the target substrate,which accounts for the parallel component of the droplet impact velocity. The weighting of the two velocity fields is expressed in terms of the impact angle:

$$\omega_r = C' \left(\alpha r + \beta r \cos\theta\right) \left(2xb - x^2\right), \tag{3.6}$$

$$\omega_\theta = -2C'\beta r \sin\theta \left(2xb - x^2\right), \tag{3.7}$$

$$\omega_x = 2C'\alpha \left(\frac{x^3}{3} - bx^2\right), \tag{3.8}$$

where C' is a time-dependent quantity and the coefficients, α and β, are the cosine and sine of the impact angle, respectively. For a normal impact ($\gamma = 0$), the present velocity field reduces to the two-dimensional velocity field proposed by Markworth and Saunders [18].

3.1.3 Splat Morphology

The deforming splat is assumed to have a uniform liquid thickness, b, which varies with time, and a limaçon perimeter. A limaçon is a curve given by the equation $r = A + B\cos\theta$, where A and B are constants. The limaçon was chosen to describe the shape of the spreading droplet because it is a simple, non-axisymmetric shape, which requires only one additional parameter (the impact angle) and resembles the

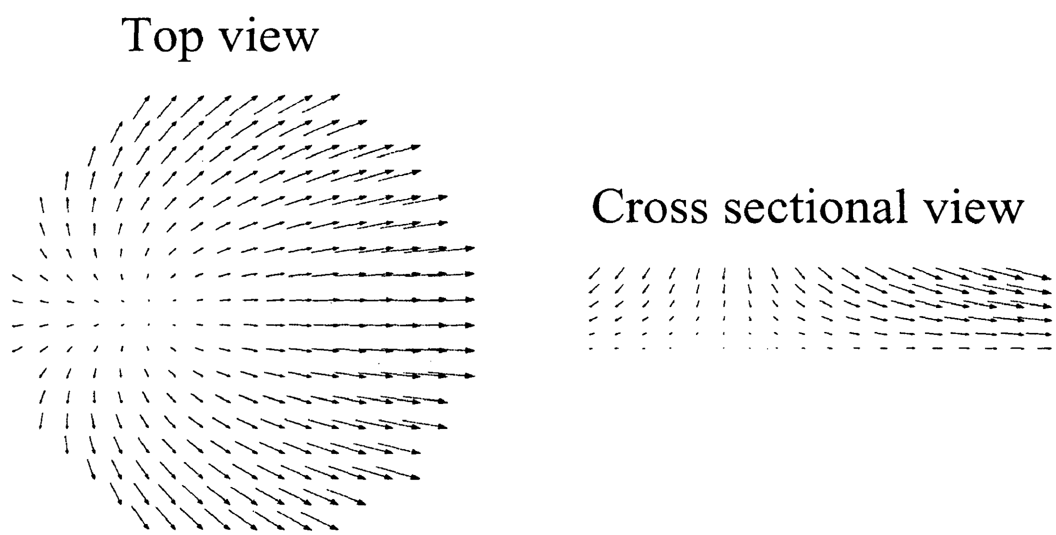

Figure 3.3: Cross sectional and top views of the imposed velocity field with a 20^o impact angle.

shape of experimentally observed splats resulting from an off-normal droplet impact [12]. Consequently, the perimeter of the spreading droplet is expressed as

$$R = f'\left(1 + \frac{\beta}{\alpha} cos\theta\right) \tag{3.9}$$

where f' is a time-dependent quantity.

The geometry of the area enclosed by the limaçon remains convex up to an impact angle roughly equal to 26^o. A concave geometry is an unphysical result, which will define an upper bound for the impact angle that can be evaluated using the present model. The limaçon used in the present model reduces to a circle in the case of a normal impact, regaining the disc-shaped splat used in Madejski's original model [16].

The size of the splat can be expressed in terms of an effective radius, R_{eff}; the radius of a circle that would encompass the same area as the limaçon used in the present study. The effective radius is introduced to enable the evaluation of the splat deformation in terms of a single dependent variable, and to be consistent with existing

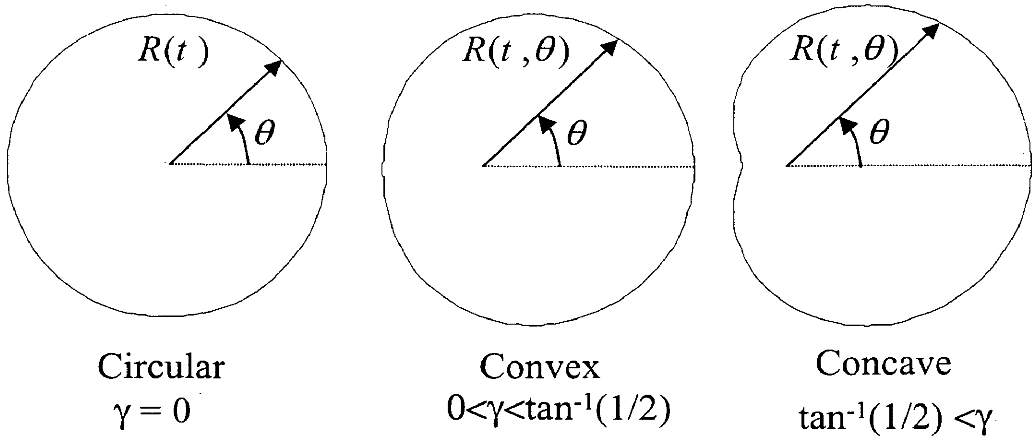

Figure 3.4: Limaçon with circular convex and concave geometries.

literature on droplet impacts. The effective radius is defined

$$R_{\text{eff}} = f'\left(1 + \frac{1}{2}\frac{\beta^2}{\alpha^2}\right)^{1/2}, \tag{3.10}$$

The time-dependent uniform liquid thickness of the splat is determined through conservation of mass:

$$b = \frac{\frac{\pi}{6}D^3 - \rho V_s}{\pi R_{\text{eff}}^2 \rho_l}, \tag{3.11}$$

where V_s is the volume of the solid. The volume of the solid is determined through equilibrium or non-equilibrium solidification models.

3.1.4 Model Formulation

The time-dependent quantity, C', may be evaluated as a function of the expansion rate, dR_{eff}/dt':

$$C' = \frac{3}{2b^2 R_{\text{eff}}}\frac{dR_{\text{eff}}}{dt'}. \tag{3.12}$$

Using Equation 3.12, and the velocity field and a splat shape chosen, Equation 3.2, Equation 3.3, and Equation 3.4 may be expressed in terms of the effective radius.

Consequently, a dimensionless form of the mechanical energy equation is obtained:

$$\frac{d}{dt}\left[\frac{3\epsilon}{10}\dot{\xi}^2\phi\left(a_1\xi^2+\frac{11}{7}\phi^2\right)+\frac{\xi}{\mathrm{We}}\left(\xi+a_2\phi\right)\right]+\frac{\xi^2\dot{\xi}^2}{\phi\mathrm{Re}}\left(a_3+a_4\frac{\phi^2}{\xi^2}\right)=0, \tag{3.13}$$

where the dimensionless variables are $\xi = R_{\text{eff}}/R_0$, $\phi = b/R_0$, $t = \omega t'/R_0$, and ϵ is the ratio of the initial effective radius, R_0, to the in-flight droplet diameter, D. The coefficients, a_i, are impact-angle-dependent and are given in Table 3.1. Furthermore, through mass conservation (Equation 3.11), the dimensionless liquid thickness may be expressed in terms of the dimensionless effective radius and the solid fraction:

$$\phi = \frac{1}{6\epsilon^2\xi^2}\left(1-f_s\right). \tag{3.14}$$

Coefficient	Normal impact	Off-normal impact
a_1	1	$\dfrac{8\alpha^6+64\alpha^4\beta^2+51\alpha^2\beta^4}{2\alpha\left(2\alpha^2+\beta^2\right)^2}$
a_2	2	$\dfrac{8\alpha^2\left(\alpha+\beta\right)}{\pi\alpha\left(2\alpha^2+\beta^2\right)^2}E\left[\dfrac{4\alpha\beta}{1+2\alpha\beta}\right]$
a_3	$\dfrac{3}{2}$	$\dfrac{3\left(16\alpha^6+152\alpha^4\beta^2+138\alpha^2\beta^4+9\beta^6\right)}{8\alpha^2\left(2\alpha^2+\beta^2\right)^2}$
a_4	$\dfrac{72}{5}$	$\dfrac{288\alpha^4+204\alpha^2\beta^2+39\beta^4}{10\alpha^2\left(2\alpha^2+\beta^2\right)}$

Table 3.1: Impact angle dependent coefficients.

The initial dimensionless effective radius, and the dimensionless liquid thickness values follow:

$$\xi(0)=1,\ \ \phi(0)=\frac{1}{6\epsilon^3}. \tag{3.15}$$

The initial expansion rate is found by equating the initial kinetic energy of the splat to that of the in-flight droplet just prior to impact:

$$\dot{\xi}(0) = \sqrt{\frac{5}{3\left[a_1 + \frac{11}{7}\left(1 + \frac{1}{2}\frac{\beta^2}{\alpha^2}\right)\frac{1}{36\epsilon^6}\right]}}. \tag{3.16}$$

The ratio of the initial effective radius to the in-flight droplet diameter, ϵ, is typically determined by equating the potential energy of the droplet prior to impact to that of the splat after impact. That relationship is expressed by a third order polynomial:

$$\epsilon^3 - \epsilon + \frac{2}{3\pi}\left(\frac{2(1+2\alpha\beta)}{\alpha^2+1}\right)^{1/2} E\left[\frac{4\alpha\beta}{1+2\alpha\beta}\right] = 0, \tag{3.17}$$

where $E[m]$ is a complete elliptic integral of the second kind,

$$E[m] = \int_0^{\pi/2} \left(1 - m\sin^2\theta\right)^{1/2} d\theta. \tag{3.18}$$

Equation 3.17 yields two positive roots for the relevant range of impact angles. The smaller of the two roots produces an initial splat height greater than the diameter of the in-flight droplet, which is unphysical, and only the larger root will be used.

To evaluate the effective radius as a function of time, Equation 3.13 is first separated into a system of first-order ordinary differential equations. That system of equations is then approximated using a fourth-order Runge-Kutta method (see Appendix A) and the initial conditions provided above.

3.1.5 Solidification Model

In order to evaluate the liquid thickness, solid growth must be determined. Madejski's original model used the Neumann solution to the Stefan solidification problem [16], which describes one-dimensional equilibrium solidification in a semi-infinite quiescent medium with perfect thermal contact at the interface. This method was adopted by Delplanque and Rangel [19] and will be used here as a baseline for equilibrium solidification with no thermal contact resistance.

Solidification is assumed to begin as soon as the droplet contacts the substrate and the location of the solid front is evaluated using the one-dimensional Stefan approximation:

$$y\left(t'\right) = 2\lambda\left(\kappa t'\right)^{1/2}, \tag{3.19}$$

where λ is a function of the Stefan number (see Appendix B), κ is the thermal diffusivity and t' is the time elapsed since the initiation of solidification at a given point (r,θ). The solid volume at time t' is evaluated by integrating the thickness of the solid over the area of the splat:

$$V_s = \pi R_0 y\left(t'\right) + 2\pi \int_0^{t'} y\left(t' - s'\right) R_{\text{eff}}\left(s'\right) \dot{R}_{\text{eff}}\left(s'\right) ds'. \tag{3.20}$$

Finally, the solid fraction may be evaluated using Equation (3.19), Equation 3.20, and mass conservation:

$$f_s = \epsilon^{5/2}\mathrm{K}_e \left[t^{1/2} + 2\int_0^t \xi\left(s\right)\dot{\xi}\left(s\right)\left(t-s\right)^{1/2} ds\right], \tag{3.21}$$

where $\mathrm{K}_e \left(= 12(\rho/\rho_l)(\lambda \mathrm{Pe}^{1/2}\right)$ is the equilibrium solidification parameter.

Experiments have shown that a significant thermal contact resistance exists at the substrate-splat interface, and heat transfer will likely be interface-limited [30]. For solidification with interface-limited heat transfer, and no superheat in the droplet prior to impact, the thickness of the solid layer can be express by a linear relationship to time (see Appendix C),

$$y\left(t'\right) = \frac{h(T_m - T_0)t'}{L\rho} \tag{3.22}$$

where h is the heat transfer coefficient between the splat and the substrate, and L is the latent heat of fusion. From Equation 3.22, Equation 3.20, and mass conservation, an expression may be determined for the solid fraction of a splat with interface-limited heat transfer:

$$f_s = \epsilon^3 \mathrm{K}_h \left[t + 2\int_0^t \left(t-s\right)\xi\left(s\right)\dot{\xi}\left(s\right) ds\right], \tag{3.23}$$

where K_h $(= 6(\rho/\rho_l)\mathrm{Ste}\ \mathrm{St})$ is a solidification parameter.

One of the benefits of the spray deposition process is the refined microstructure resulting from rapid solidification. Hence, the effects of rapid solidification must be included. However, if the cooling rate is large enough that solidification will be kinetically driven, an explicit solution for the solid thickness as a function of time may not be found, and a different approach must be taken. A lumped parameter method is used for the thermal energy conservation in the splat. This approach is valid though much of the solidification process but may loose some accuracy during recalescence, because of the high solidification rate. This effect will cause an underestimate of the solid-liquid interface temperature and result in a higher solidification rate during recalescence. However, the accuracy of this assumption is consistent with the accuracy of the current model.

The temperature of the splat is evaluated with a global thermal energy balance. If m is the mass of the splat, c is the specific heat, ρ_s is the solid density and L is the latent heat of fusion, the thermal energy balance is given by

$$mc\frac{dT}{dt'} = -hA\left(T - T_s\right) + \rho L\frac{dV_s}{dt'}, \tag{3.24}$$

where T is the splat temperature, and T_s is the substrate temperature. For the themal energy balance above, the free surface is assumed to be adiabatic. Furthermore, The rate of change of the solid volume, dV_s/dt', is evaluated using a linear approximation to the kinetic solid growth rate, which is valid for small undercooling [24]:

$$\frac{dy}{dt'} = \mu_k(T_m - T), \tag{3.25}$$

where μ_k is a kinetic parameter relating the velocity of the solid-liquid interface to the degree of undercooling, and T_m is the splat equilibrium melting temperature. The solid is assumed to grow axially at a velocity that is uniform over the area of the splat. Consequently, an expression for the rate of change of the solid volume may be determined from the velocity of the solid-liquid interface:

$$\frac{dV_s}{dt'} = \pi R_{\text{eff}}^2 \mu_k \left(T - T_m\right), \tag{3.26}$$

Equation 3.24 and Equation 3.26 may be evaluated in dimensionless terms to give

$$\frac{d\Theta}{dt} = \frac{6\epsilon^3\xi^2}{1 + f_s\left(r_c - 1\right)}\left[\frac{K_{ne}}{\text{Ste}}\left(1 - \Theta\right) - \text{St}\Theta\right], \tag{3.27}$$

and

$$\frac{df_s}{dt} = 6\epsilon^3\xi^2 K_{ne}\left(1-\Theta\right), \tag{3.28}$$

where $\Theta\,(=(T-T_0)\,/\,(T_m-T_0))$ is the dimensionless splat temperature, r_c is the ratio of the solid specific heat to the liquid specific heat and $K_{ne}\,(=(\rho/\rho_l)\mu_k(T_m-T_s)/\omega)$ is a non-equilibrium solidification parameter. $\mathrm{Ste}\,(=c_l(T_m-T_s)/L)$ is the Stefan number and $\mathrm{St}\,(=h/(\rho_l c_l \omega)$ is the Stanton number.

Due to the high cooling rates involved in the spray deposition process, appreciable undercooling may be achieved. Consequently, the splat will experience liquid cooling until the nucleation temperature is reached. The nucleation temperature depends on the cooling rate, the droplet size and the nucleation rate. This dependence is expressed through Hirth's equation [31]:

$$\frac{0.01I\left(\pi D^3/6\right)\Delta T_0}{-\frac{dT}{dt'}} = 1, \tag{3.29}$$

where I is the nucleation rate and $\Delta T_0(=T_m-T_N)$ is the undercooling. The heterogeneous nucleation rate is [32]

$$I = \frac{n_s}{n}N\exp\left[-\frac{16\pi}{3}\frac{\sigma_{cl}^3}{\rho_l L k_B}\frac{T_m^2}{\left(T_m-T_n\right)^2 T_n}\psi\left(\lambda_c\right)\right], \tag{3.30}$$

where n is the number of molecules in the liquid per unit volume, n_s' is the number of liquid-substrate surface atoms in the liquid per unit volume, σ_{cl} is the crystal liquid surface energy, k_B is the Boltzmann constant and $N\,(\approx 10^{33}m^{-3}s^{-1})$ [32] depends on the critical nucleus size and surface energy. The function,

$$\psi\left(\lambda_c\right) = \frac{1}{4}\left(2+\cos\lambda_c\right)\left(1-\cos\lambda_c\right)^2, \tag{3.31}$$

where λ_c is the substrate-crystal-liquid contact angle measured through the crystal, approaches zero as the contact angle goes to zero. Consequently, the barrier to nucleation will vanish as this contact angle approaches zero, and no undercooling will occur. The heterogeneous nucleation rate depends heavily on the exponential term; hence, the pre-exponential term may vary by several orders of magnitude with little effect. Hirth's equation may be expressed in dimensionless form as

$$\Theta_N = \frac{6\epsilon^4}{0.01\pi\Im}\frac{d\Theta}{dt} + 1, \tag{3.32}$$

where Θ_N is the dimensionless nucleation temperature, and the dimensionless nucleation rate, $\Im$, is given by

$$\Im = 6\epsilon^3\xi^2\delta\eta\exp\left[-\frac{16\pi}{3}K_N\frac{(1+\Lambda)^2}{(1-\Theta)^2(\Theta+\Lambda)}\psi(\lambda_c)\right], \tag{3.33}$$

where δ is the ratio of the atomic diameter to the in-flight droplet diameter, the coefficient $K_N\ (= \sigma_{lc}^3/[\rho^2 L^2 k_B(T_m - T_s))$ is a nucleation parameter, $\Lambda = T_s/[T_m - T_s]$, and $\eta = NR_0^4\omega$.

3.2 Results and Discussion

Three physical mechanisms influence droplet spreading: viscous dissipation, transfer of kinetic energy to potential energy and solidification. A parametric study was conducted to study the influence of the impact angle by varying the dimensionless parameters that characterize each of these mechanisms (Weber number, Reynolds number or the solidification parameter) while holding the other two parameters constant. For this investigation the Neumann solidification model is used (Equation 3.21). The Reynolds number was varied from 400 to 400,000, the Weber number from 5 to 500 and the solidification parameter from 0.02 to 5.0. These values correspond to possible applications of this model, such as thermal spraying and splat quenching [19]. Even though the upper values of the Reynolds number a large, the flow in these cases will remain laminar, because the splat liquid thickness is the relevent dimension for the flow turbulence, not the droplet diameter. The spreading and solidification process is evaluated for each case for impact angles ranging from 0 to 20^o. The emphasis of this discussion is on the effect of non-zero impact angles on predicted droplet behavior. Therefore, this influence is assessed over the relevant range for each pertinent dimensionless parameter (Re,We, K_e).

Thermal contact resistance and rapid solidification play a significant role in droplet solidification, and consequently in droplet spreading dynamics. The influences of thermal contact resistance and rapid solidification are evaluated for the spreading and solidification of aluminum droplets impacting normally to the target substrate. Thermal contact resistance is evaluated with the linear approximation for the solid front position (Equation 3.23), and undercooling is evaluated using the lumped parameter model (Equation 3.27 and Euaqtion 3.28). To evaluate the influence of thermal contact resistance, the Stanton number is varied between 1.65×10^{-3} to 1.65×10^{-1}. The influence of rapid solidification is investigated by varying the degree of undercooling with the substrate-crystal-contact angle. The contact angle is varied between 0 and 90^o.

3.2.1 Influence of Droplet Impact Angle

First, the influence of impact angle on the spreading droplet was investigated for the reference case (Re = 400, We = 500, K = 0.02). In this case, viscous dissipation is found to be the dominant phenomenon in controlling droplet spreading. The dissipated energy is an order of magnitude greater than the change in potential energy over the range of relevant impact angles.

The results in Figure 3.5 are evaluated using the in-flight droplet radius, R_d, as the reference length rather than the initial effective radius, R_0. R_d was chosen as the reference length, rather than R_0, as is typical in literature, because R_0 is a function of the impact angle if potential energy is to be conserved. While the variation in R_0 is negligible, R_d provides a more consistent reference length.

It was found that the final effective radius, the average expansion rate and the final solid fraction all decrease as the impact angle increases (Figure 3.5). The final effective radius for an impact angle of 20^o was roughly 8% lower than that of a normal impact and the final solid fraction of the splat was about 3% lower. This corresponds to a final splat liquid thickness that is about 16% greater. These results indicate, for the reference case, that higher impact angles produce less efficient droplet spread and solidification, with regard to splat coverage.

These results can be interpreted from an energetic point of view. It was found that increasing the impact angle causes the total energy dissipated at a given effective radius to increase with very little change in the potential energy (Figure 3.6). As the effective radius to increases, the difference in dissipated energy is more significant indicating a consistently higher rate of viscous dissipation with respect to the splat radius. As the impact angle is increased, a larger portion of the kinetic energy in the slat contributes to displacement (the droplet center of mass is moving during spreading after an angled impact) rather than expansion alone. This results in a greater degree of dissipation for a given value of the effective splat radius. The dominant role of viscous dissipation in the reference case and the increase in viscous dissipation at higher impact angles result in a significant decrease in impact efficiency at higher impact angles.

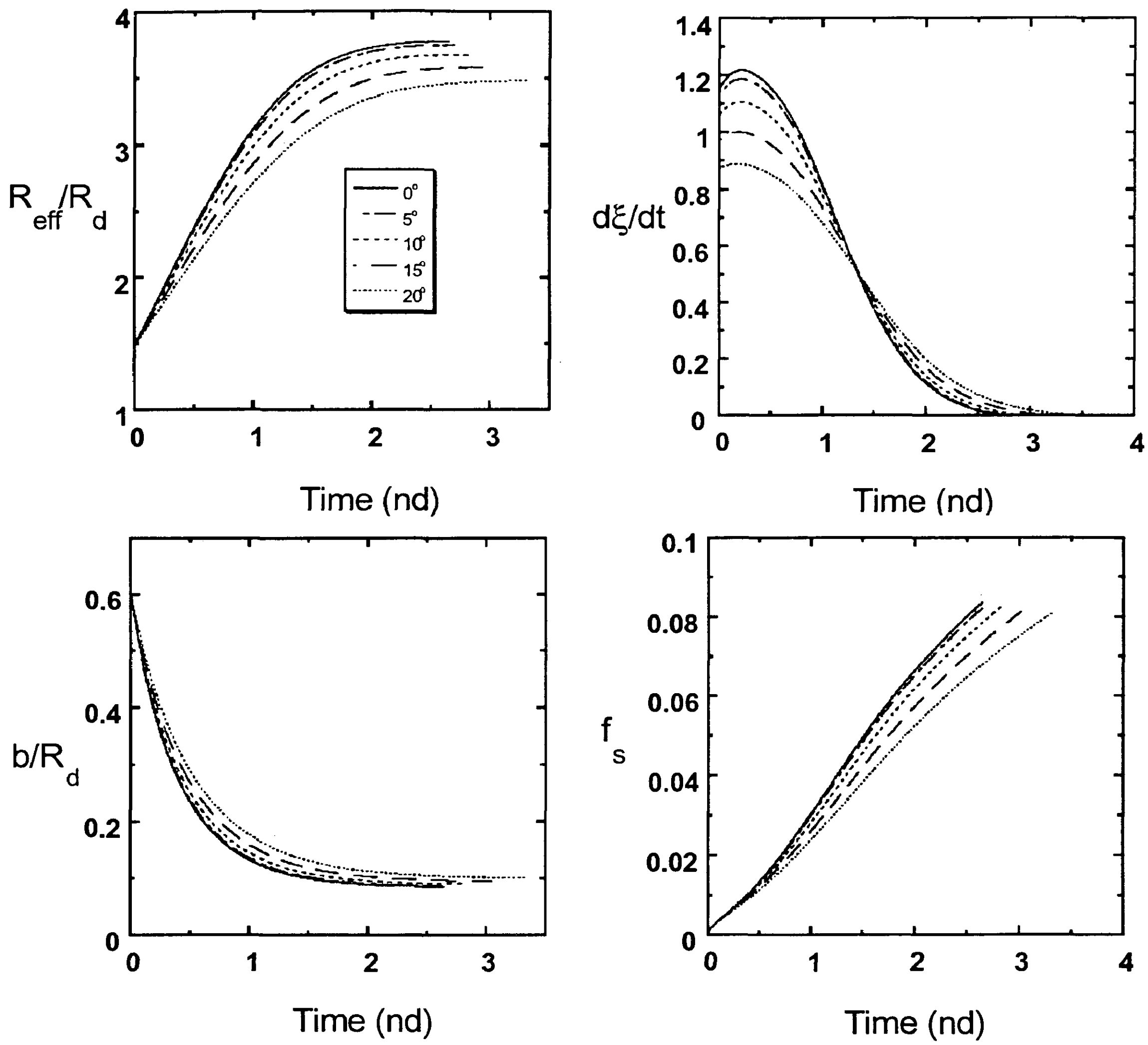

Figure 3.5: Splat dimensions for Re=400, We=500 and K=0.02 for impact angles ranging from 0 to 20^o.

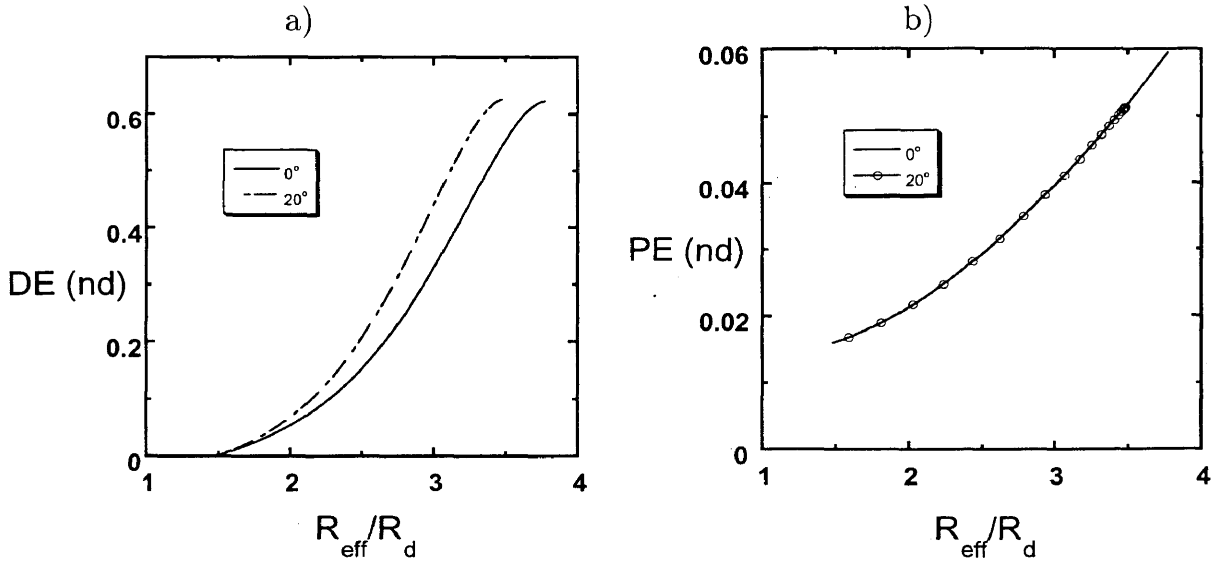

Figure 3.6: Comparison of energy of a Re=400, We=500 and K=0.02 impact: a)dissipated and b) potential, for impacts of 0 and 20^o.

As the Reynolds number is increased the role of viscous dissipation on the splat spreading and solidification process diminishes. The total amount of energy dissipated, for a normal impact, with a Reynolds number of $400,000$, Weber number of 500 and solidification parameter of 0.02, was found to be roughly twice the increase in potential energy. This is to be compared with dissipation energy being an order of magnitude greater than the change in potential energy for the reference case.

Again the final splat effective radius was found to decrease for higher impact angles. The splat completely solidified for all impact angles, a result of very thin splats formed with a Reynolds number of $400,000$. The final splat effective radius was found to decrease by roughly 6% for an impact angle of 20^o as compared to a normal impact.

The decrease in the effective radius of the final splat as the impact angle is increased is relatively less pronounced than that of the reference case. This trend is observed for Reynolds numbers ranging from 400 to $400,000$ (Figure 3.7). The results in Figure 3.7 are normalized by the final effective radius at a normal impact for the specified Reynolds numbers. As in the reference case, for increasing impact angles the amount of energy dissipated increased for a given effective radius. However, for higher

Reynolds numbers the influence of viscous dissipation is diminished, accounting for the decrease in the relative effects of higher impact angles.

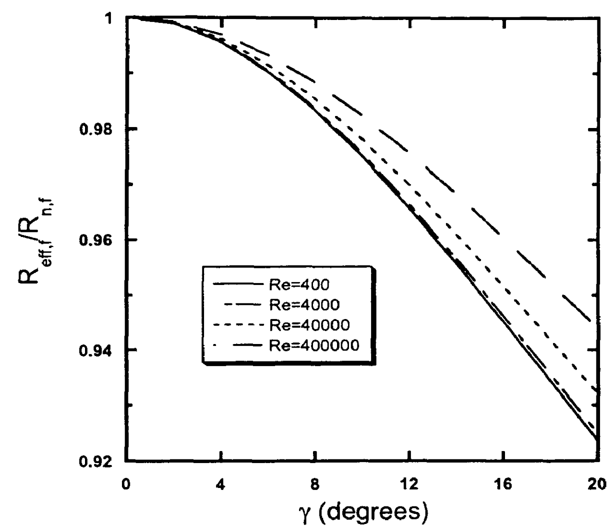

Figure 3.7: Relative variation of final splat effective radius as a function of impact angle for We=500, K=0.02 for various Reynolds numbers, normalized by the final effective radius for a normal impact under the same conditions.

At lower Weber numbers the influence of surface tension becomes more prominent, increasing the transfer of kinetic energy to potential energy during splat deformation and solidification. The increase in potential energy for a normal impact, with a Weber number of 20, Reynolds number of 400 and solidification parameter of 0.02, is an about three times greater than energy lost through viscous dissipation. The final splat effective radius was found to decrease for this case at higher impact angles. The final splat effective radius decreased by roughly 3% for an impact angle of 20^o while, the final time increased as in the reference case.

A reduction of the relative effect of the impact angle is seen for Weber numbers ranging from 5 to 500 as the Weber number decreases (Figure 3.8). The results in Figure 3.8 are normalized by the final effective radius at a normal impact for the specified Weber numbers. The reduction of the relative effect of the impact angle is attributed to a increase in the potential energy at lower Weber numbers and consequently a decrease in the role of viscous dissipation.

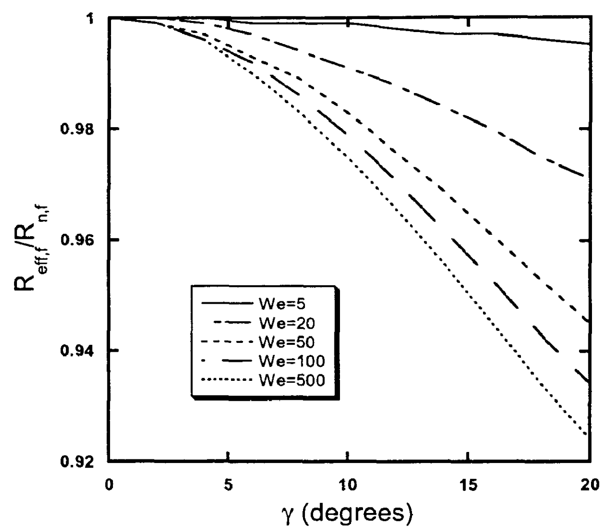

Figure 3.8: Relative variation of final splat effective radius as a function of impact angle for Re=400, K=0.02 for various Weber numbers, normalized by the final effective radius for a normal impact under the same conditions.

A high value of the solidification parameter increases the rate of solidification and can results in a smaller final splat radius. As the solidification parameter is increased, the role of viscous dissipation becomes even more prominent than in the reference case because faster solidification results in a relatively thinner liquid layer at a given stage of the spreading history, which increases the velocity gradient in the fluid layer, and thus the shear stress. The energy dissipated in a normal impact was found to be 17 times greater than the change in potential energy for a Reynolds number of 400, Weber number of 500 and solidification parameter of 0.5, while the dissipated energy was 14 times greater for the reference case.

As in the reference case, the high Reynolds number case, and the low Weber number case the final effective splat radius was found to decrease as the impact angle increased. The relative effect of increasing the impact angle diminished as the solidification parameter increased. This trend is observed for solidification parameters ranging from 0.02 to 5.0 (Figure 3.9). The results in Figure 3.9 are normalized by the final effective radius at a normal impact for the specified solidification parameters. The decrease in the relative effect of the impact angle would seem to contradict earlier trends, attributed to the increasing significance of viscous dissipation for higher value of K. Here, the dissipated energy, for a given effective radius, is still greater for higher impact angles and it has been stated that this difference increases with the effective radius. However, higher solidification parameters result in smaller splats and a lower difference in the total amount of energy dissipated at the final splat effective radius.

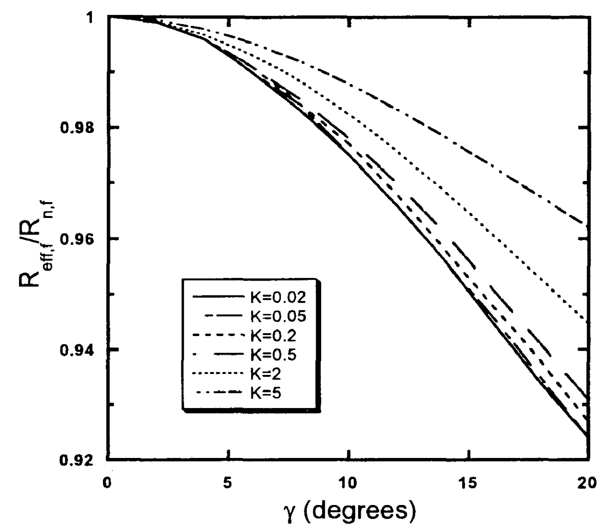

Figure 3.9: Relative variation of final splat effective readius as a function of impact angle for Re=400, We=500, and various values of K, normalized by the final effective radius for a normal impact under the same conditions.

3.2.2 Influence of Thermal Contact Resistance

Thermal contact resistance is neglected when the Neumann solution to the Stefan solidification problem is used. However, in actual processes the contact between the splat and substrate will be less than perfect, due to gas and vapor trapped between the splat and substrate. The quality of the contact between the splat and the substrate will be particularly influenced by the roughness of the substrate and the wettability of the substrate with respect to the splat material.

Cases were run for an aluminum droplet impacting normally on a cold substrate with no initial superheat. The heat transfer coefficient between the substrate and the splat was varied between 10^4 and 10^6 $Wm^{-2}K^{-1}$ [21] and compared to a case with perfect thermal contact. Each case was run with Re = 2860, We = 83.6, Ste = 1.44, and St was varied from 1.65×10^{-3} to $1.65 \times 10^{-}1$. Solidification was model using Equation 3.23 for the cases with thermal contact resistance and Equation 3.21 for the case with perfect contact.

The results indicate that the solidification rate is significantly influenced by the heat transfer coefficient between the substrate and splat (Figure 3.10). Wang and Matthys [21] found that the heat transfer coefficient may vary significantly; hence the heat transfer coefficient was varied by two orders of magnitude. Furthermore, it is seen that the higher rate of solidification plays a significant roll in splat deformation (Figure 3.10). Higher solidification rates increase the rate of viscous dissipation, hindering the growth of the splat. While, the thermal contact resistance is not a well-known quantity it is seen to play a significant roll in the spray deposition process. Furthermore, while the Neumann solution to the Stefan solidification problem has been used in several droplet impact studies, it should be viewed only as a limiting case for solidification.

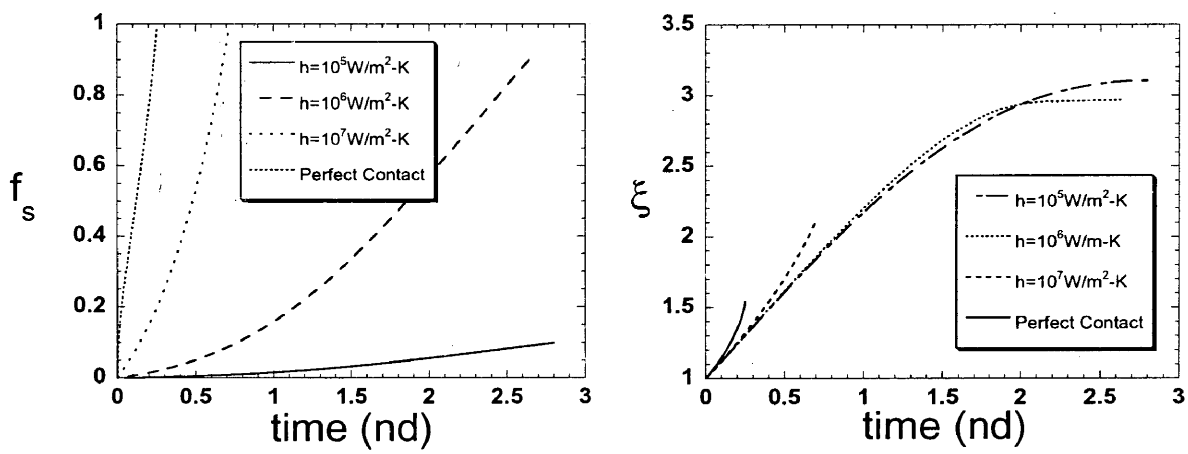

Figure 3.10: Comparison of spreading and solidification of an aluminum droplet with various heat transfer coefficients.

3.2.3 Influence of Undercooling

Due to the high cooling rates involved in the spray deposition process, it is likely that significant undercooling may occur in the splat [21]. The nucleation barrier that results in undercooling is reduced by heterogeneous nucleation at the substrate. The nucleation barrier is influenced by the substrate-crystal-liquid contact angle [32]. As the contact angle approaches zero, the barrier to nucleation vanishes and no undercooling will occur.

Three cases were run with the substrate-crystal-liquid contact angle varied between 0 and 90^o. The results were run with the same parameters as were used in the study of thermal contact resistance but including the influence of undercooling. The additional parameters $K_n = 40$ and $K_N = 0.792$ were used for the solidification rate and nucleation.

The results indicate that, as the contact angle increases, there is an increase in the degree of undercooling, resulting in a delay of recalescence, and that no under cooling will occur for complete wetting of the substrate by the crystal (Firgure 3.11), as was expected. it is shown that increasing the degree of undercooling in the splat will increase the size of the final solidified splat. Undercooling increases the maximum coverage of the solidified splat by delaying the solidification time, and the resulting increase in viscous dissipation.

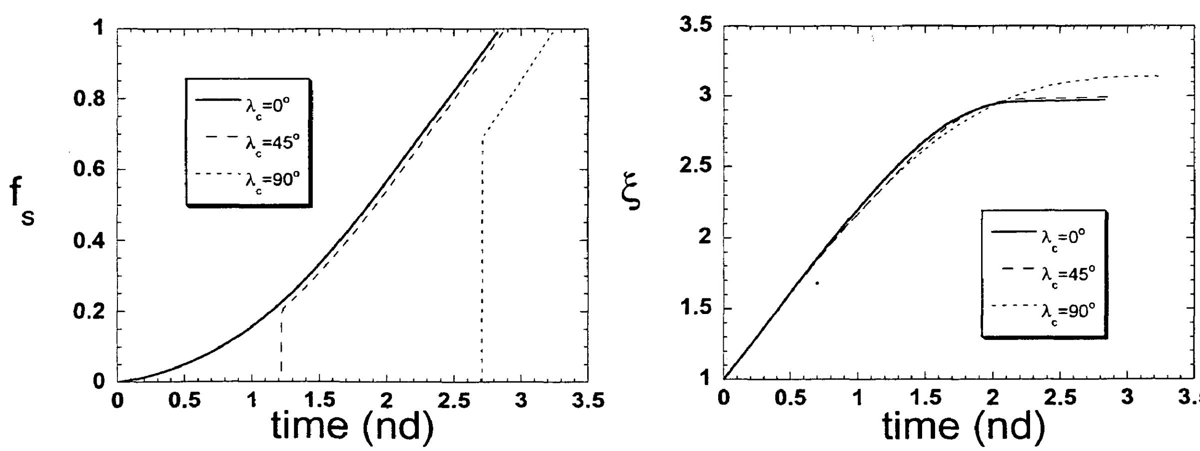

Figure 3.11: Comparison of spreading and solidification of an aluminum droplet with various levels of undercooling.

3.2.4 Discussion

Aziz *et al.* [26], obtained experimental results of molten tin droplets impinging on a stainless steel substrate. Individual droplets were generated and allowed to fall under the effects of gravity. A single photograph was taken of each droplet. The spreading history of the droplet was then reconstructed from several impacts.

Results from the analytical model, and the modified version of RIPPLE are compared to experimental results obtained by Aziz *et al.* [26], for a 2.7mm tin droplet impacting a cold substrate at 2.0m/s (Figure 3.12). It is seen that the degree of spreading predicted by the numerical model more closely resembles that of the experimental results. The analytical model over predicted the maximum spread of the droplet by roughly 45%, which is consistent with other analytical models [15].

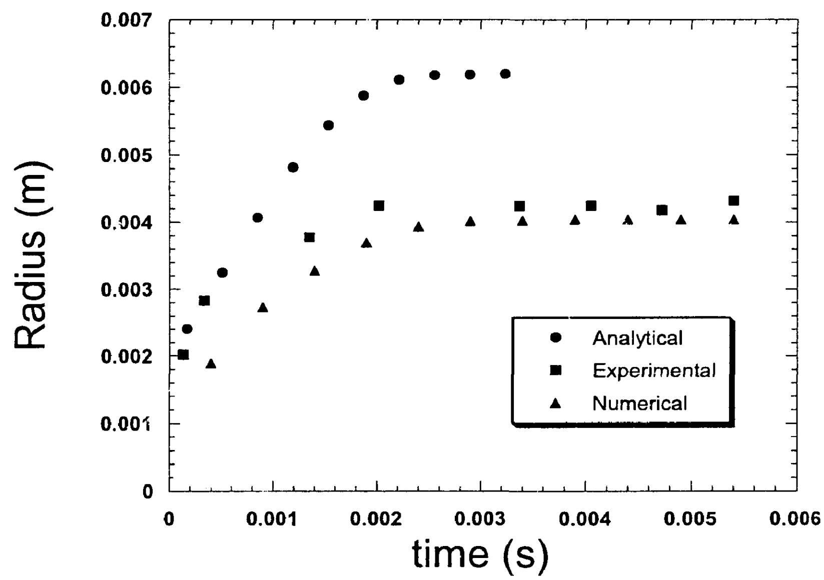

Figure 3.12: Comparison of analytical and numerical results with experimental data [26] for the spreading and solidification of a tin droplet impacting a cold substrate.

It has been discussed that a major source of error in the analytical model resides in the initial conditions. The initial expansion rate is found by equating the initial kinetic energy to that of the droplet just prior to impact. However, the initial shape and velocity field imposed on the droplet are more representative of a droplet that has already experienced significant deformation, and consequently, a significant reduction in the kinetic energy of the droplet. It is proposed that rather than equating the initial kinetic energy to that of the droplet just prior to impact, the initial kinetic energy should be set to a fraction of the kinetic energy of the droplet just prior to impact.

The fraction of the initial kinetic energy remaining when the splat reaches a radius equal to the initial radius in the analytical model was calculated from the simulation results, and found to be 38%. The results from the analytical model were then recalculated using a corrected initial kinetic energy. This correction was found to significantly improve the agreement between the analytical model and the experimental results (Figure 3.13). However, the analytical model must be self-contained, and consequently, the correction to the initial conditions must eventually be related to the model itself.

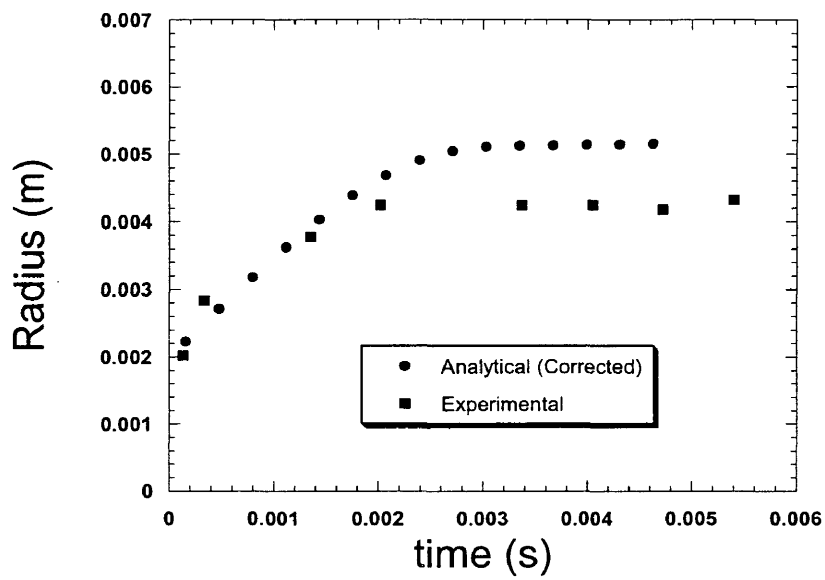

Figure 3.13: Comparison of corrected analytical, and experimental data [26] for the spreading and solidification of a tin droplet impacting a cold substrate.

While the numerical procedure clearly yields more accurate results than the analytical model, it is also very computationally intensive, requiring more than three CPU hours on a 600 MHz Pentium III processor to evaluate a single droplet impact, as compared to seconds for the analytical model. Also, the analytical model more readily offers insight into the physical mechanisms influencing droplet spreading and solidification. However, the numerical model has been shown above to be a valuable method for the evaluation and improvement of the analytical model, due to the accuracy and detail obtained.

A semi-analytical model based on energy conservation was developed to investigate the effects of droplet impact angle on splat spreading and solidification. To this end, a three dimensional velocity field and non-axisymmetric shape were prescribed. The derivation of the mechanical energy balance by Delplanque and Rangel [19] was expanded to accommodate the three-dimensional flow field. The model predicts an increase in the mechanical energy lost to viscous dissipation for a given splat size at higher impact angles. The influence of impact angle on energy re-distribution results in smaller solidified splats at higher impact angles. This reduction in final splat expansion is less significant as the influence of viscous dissipation diminishes. Solidification models including the influence of thermal contact resistance and under cooling where incorporated. Increased thermal contact resistance was seen to increase the final splat size by hindering solidification and higher levels of undercooling resulted in an increased final splat size by delaying the increase in viscous dissipation associated with solidification.

CHAPTER 4

CONCLUDING REMARKS

Spray rolling is an efficient technique for the production of aluminum strip. The commercial viability of the spray rolling process requires a thorough understanding of the various physical mechanisms involved. Furthermore, the spreading and solidification of individual droplets has a significant influence on the final material quality in the spray rolling process. Hence, numerical, and analytical models have been developed to investigate spreading and solidification of a single droplet impinging on a solid substrate.

The numerical procedure developed involved the implementation of an energy solver, based on an enthalpy formulation of the thermal energy conservation equation, in an existing Navier-Stokes solver for incompressible free surface flows (RIPPLE). The modified version of RIPPLE was compared to several test cases, and shown to have a wide range of validity, with respect to droplet impact problems.

The analytical model developed uses an integral method, based on a mechanical energy balance. A three-dimensional velocity field and a non-axisymmetric shape are imposed to adequately model off-normal droplet impacts. Furthermore, three solidification models were presented including: equilibrium solidification with no thermal contact resistance, equilibrium solidification with thermal contact resistance, and rapid solidification with thermal contact resistance. The model predicts that at higher impact angle, smaller solidified splat will be produced, and that thermal contact resistance will significantly affect droplet solidification and spreading. Furthermore, it was shown that undercooling will affect the size of the final solidified splat by delaying the increase in viscous dissipation associated with solidification.

While the numerical and analytical models presented here are valuable tools for the evaluation of droplet impacts, there are aspects of droplet deposition in the spray-rolling process that can not be evaluated with the models presented here. First, these models assume that the droplet is fully liquid when it first comes in contact with the substrate; however, in the spray-rolling process, droplets will typically have a significant solid fraction prior to impact. The initial solid fraction may be included in the current analytical model by assuming the solid is located at the bottom of the splat, but a more accurate approach would require analysis with the visco-elastic stress-strain relationship. Furthermore, droplets may impact previously deposited material that has not completely solidified, which the current models due not account for. Furthermore, the influences of the impact angle, as studied with the analytical model, can not be validated using the current axisymmetric numerical model. However, a three-dimensional code for free surface flow (TRUCHAS) is currently under development at Los Alamos National Laboratory, which may eventually be used to validate the off-normal droplet impact model and study the influences of other three-dimensional aspects of droplet impact, such as splashing and impact on irregular surfaces.

REFERENCES CITED

[1] D.B. Kothe. Review of computional fluid dynamics with moving boundaries. *AIAA Journal*, 36:303–304, 1998.

[2] T. Watanabe, I. Kuribayashi, T. Honda, and A. Kanzawa. Deformation and solidification of a droplet on a cold substrate. *Chemical Engineering Science*, 47(12):3059–3065, 1992.

[3] M. Sussman and C.F. Edwards. A level set approach for computing solutions to incompressible two-phase flow. *Journal of Computational Physics*, 114:146–159, 1994.

[4] W.J. Rider and D.B. Kothe. Stretching and tearing interface tracking methods. In *12th AIAA CFD Conference*, 1995.

[5] D.J.E. Harvie and D.F. Fletcher. A new volume of fluid advection algorithm: the stream scheme. *Journal of Computational Physics*, 162:1–32, 2000.

[6] S.W.J. Welche and J. Wilson. A volume of fluid based method for fluid flows with phase change. *Journal of Computational Physics*, 160:662–682, 2000.

[7] D.B. Kothe, R.C. Mjolsness, and M.D. Torrey. *RIPPLE: A Computer Program for Incompressible Flows with Free Surfaces.* Los Alamos National Laboratory, Los Alamos, New Mexico 87545.

[8] J.M. Waldvogel and D. Poulikakos. Solidification phenomena in picoliter size solder droplet deposition on a composite substrate. *International Journal of Heat and Mass Transfer*, 40(2):295–309, 1997.

[9] J.-P. Delplanque and R.H. Rangel. A comparison of models, numerical simulation, and experimental results in droplet deposition processes. *Acta materialia*, 46(14):4925–4933, 1998.

[10] H. Zhang. Theoretical analysis of spreading and solidification of molten droplet during thermal spray deposition. *International Journal of Heat and Mass Transfer*, 42:2499–2508, 1999.

[11] M. Pasandideh-Fard, R. Bhola, S. Chandra, and J. Mostaghimi. Deposition of tin droplets on a steel plate: simulations and experiments. *International Journal of Heat and Mass Transfer*, 41:2929–2945, 1998.

[12] M. Bussmann, J. Mostaghimi, and Chandra S. On a three-dimensional volume tracking model of droplet impact. *Physics of Fluids*, 11(6):1406–1417, 1999.

[13] D.B. Kothe and R.C. Mjolsness. Ripple - a new model for incompressible flows with free surfaces. *AIAA Journal*, 30:2694–2700, 1992.

[14] H.G. Fan and R. Kovacevic. Droplet formation, detachment, and impingement on the molten pool in gas metal arc welding. *Metallurgical and Materials Transactions B*, 30B:791–801, August 1999.

[15] W.M. Healy, J.G. Hartley, and S.I. Abdel-Khalik. Comparison between theoretical models and experimental data for the spreading of liquid droplets impacting a solid surface. *International Journal of Heat and Mass Transfer*, 39(14):3079–3082, 1996.

[16] J. Madejski. Solidification of droplets on a cold surface. *International Journal of Heat and Mass Transfer*, 19:1009–1013, 1976.

[17] H.S. Carslaw and J.C. Jaeger. *Conduction of Heat in Solids.* Oxford: Clarendon Press, 1959.

[18] A.J. Markworht and J.H. Saunders. An improved velocity field for the madejski splat-quench solidification model. *International Journal of Heat and Mass Transfer*, 35(7):1836–1837, 1992.

[19] J.-P. Delplanque and R.H. Rangel. An improved model for droplet solidification on a flat surface. *Journal of Materials Science*, 32(6):1519, 1997.

[20] V.V. Sobolev and J.M. Guilemany. Influence of droplet impact angle on droplet-substrate mechanical interaction in thermal spraying. *Materials Letters*, 33:315–319, 1998.

[21] G.-X. Wang and E.F. Matthys. Modeling of nonequilibrium surface melting and resolidification for pure metals and binary alloys. *Journal of Heat Transfer*, 118:944–951, November 1996.

[22] J.-P. Delplanque, E.J. Lavernia, and R.H. Rangel. Analysis of in-flight oxidation during reactive spray atomization and deposition processing of aluminum. *Journal of Heat Transfer*, 122(1):126–133, 2000.

[23] R. Mehrabian. Rapid solidification. *International Metals Reviews*, 27(4):185–208, 1982.

[24] G.-X. Wang and E.F. Matthys. Numerical modelling of phase change and heat transfer during rapid solidification processes: use of control volume integrals with element subdivision. *International Journal of Heat and Mass Transfer*, 35(1):141–153, 1992.

[25] M. Chung and R.H. Rangel. Simulation of metal droplet deposition with solidification including undercooling and contact resistance effects. *Numerical Heat Transfer, Part A*, 37:201–226, 2000.

[26] S.D. Aziz and S. Chandra. Impact, recoil and splashing of molten metal droplets. *International Journal of Heat and Mass Transfer*, 43:2841–2857, 2000.

[27] F.P. Incropera and D.P. DeWitt. *Fundamental of Heat and Mass Transfer*. John Wiley and Sons, fourth edition edition, 1996.

[28] R.J. Kee, M.E. Coltrin, and P. Glarborg. *Theoretical and Practical Aspects of Chemically Reacting Flow Modeling.*

[29] S. Annavarapu, D. Apelian, and A. Lawley. *Metall. Trans*, 19(A):3077, 1988.

[30] W. Liu, G.X. Wang, and E.F. Matthys. Thermal analysis and measurements for a molten metal drop impacting on a substrate: colling, solidification and

heat transfer coefficient. *International Journal of Heat and Mass Transfer*, 28(8):1387–1395, 1995.

[31] J.P. Hirth. Nucleation, undercooling and homogeneous structures in rapidly solidified powders. *Metallurgical Transactions A*, 9A:401–404, March 1978.

[32] Merton C. Flemings. *Solidification Processing*. McGraw-Hill, 1974.

APPENDIX A

NUMERICAL SOLUTION OF INTEGRO-DIFFERENTIAL EQUATION

A fourth-order Runge-Kutta method is used to solve the system of differential equations defined by the analytical droplet impact model (Chapter 3). First, the mechanical energy balance is divided into a system of first-order differential equations. A new variable is defined to be equal to the expansion rate ($\eta = \dot{\xi}$) giving

$$\dot{\xi}\left(t\right) = F_1\left(\eta\left(t\right)\right). \tag{A.1}$$

The rate of change of η can then be define by Equation 3.13 to give

$$\dot{\eta}(t) = F_2\left(\xi\left(t\right), \dot{\xi}\left(t\right), \Theta\left(t\right), f_s\left(t\right)\right). \tag{A.2}$$

The rate of change of the temperature in the droplet is defined by Equation 3.27 such that

$$\dot{\Theta}\left(t\right) = F_3\left(\xi\left(t\right), \Theta\left(t\right), f_s\left(t\right)\right), \tag{A.3}$$

and the rate of change of the solid fraction can be defined by Equation 3.28,

$$\dot{f}_s\left(t\right) = F_4\left(\xi\left(t\right), \Theta\left(t\right)\right). \tag{A.4}$$

The solution may be advanced in time using the equations below.

$$\xi\left(t_0 + \delta t\right) = \xi\left(t_0\right) + K_1, \tag{A.5}$$

$$\eta\left(t_0 + \delta t\right) = \eta\left(t_0\right) + K_2, \tag{A.6}$$

$$\Theta\left(t_0 + \delta t\right) = \Theta\left(t_0\right) + K_4, \tag{A.7}$$

$$f_s\left(t_0 + \delta t\right) = f_s\left(t_0\right) + K_4, \tag{A.8}$$

where

$$K_i = \frac{K_{i,1} + 2K_{i,2} + 2K_{i,3} + K_{i,4}}{6}. \tag{A.9}$$

The coefficients, $K_{i,j}$, are given by the following equations:

$K_{1,1} = \frac{\delta t}{2} F_1 \left(\eta \left(t_0\right)\right)$
$K_{2,1} = \frac{\delta t}{2} F_2 \left(\xi \left(t_0\right), \eta \left(t_0\right), \Theta \left(t\right), f_s \left(t_0\right)\right)$
$K_{3,1} = \frac{\delta t}{2} F_3 \left(\xi \left(t_0\right), \Theta \left(t_0\right), f_s \left(t_0\right)\right)$
$K_{4,1} = \frac{\delta t}{2} F_4 \left(\xi \left(t_0\right), \Theta \left(t_0\right)\right)$
$K_{1,2} = \frac{\delta t}{2} F_1 \left(\eta \left(t_0 + K_{2,1}\right)\right)$
$K_{2,2} = \frac{\delta t}{2} F_2 \left(\xi \left(t_0 + K_{1,1}\right), \eta \left(t_0 + K_{2,1}\right), \Theta \left(t_0 + K_{3,1}\right), f_s \left(t_0 + K_{4,1}\right)\right)$
$K_{3,2} = \frac{\delta t}{2} F_3 \left(\xi \left(t_0 + K_{1,1}\right), \Theta \left(t_0 + K_{3,1}\right), f_s \left(t_0 + K_{4,1}\right)\right)$
$K_{4,2} = \frac{\delta t}{2} F_4 \left(\xi \left(t_0 + K_{1,1}\right), \Theta \left(t_0 + K_{3,1}\right)\right)$
$K_{1,3} = \frac{\delta t}{2} F_1 \left(\eta \left(t_0 + K_{2,2}\right)\right)$
$K_{2,3} = \frac{\delta t}{2} F_2 \left(\xi \left(t_0 + K_{1,2}\right), \eta \left(t_0 + K_{2,2}\right), \Theta \left(t_0 + K_{3,2}\right), f_s \left(t_0 + K_{4,2}\right)\right)$
$K_{3,3} = \frac{\delta t}{2} F_3 \left(\xi \left(t_0 + K1, 2\right), \Theta \left(t_0 + K_{3,2}\right), f_s \left(t_0 + K_{4,2}\right)\right)$
$K_{4,3} = \frac{\delta t}{2} F_4 \left(\xi \left(t_0 + K_{1,2}\right), \Theta \left(t_0 + K_{3,2}\right)\right)$
$K_{1,4} = \frac{\delta t}{2} F_1 \left(\eta \left(t_0 + K_{2,3}\right)\right)$
$K_{2,4} = \frac{\delta t}{2} F_2 \left(\xi \left(t_0 + K_{1,3}\right), \eta \left(t_0 + K_{2,3}\right), \Theta \left(t_0 + K_{3,3}\right), f_s \left(t_0 + K_{4,3}\right)\right)$
$K_{3,4} = \frac{\delta t}{2} F_3 \left(\xi \left(t_0 + K_{1,3}\right), \Theta \left(t_0 + K_{3,3}\right), f_s \left(t_0\right)\right)$
$K_{4,4} = \frac{\delta t}{2} F_4 \left(\xi \left(t_0 + K_{1,3}\right), \Theta \left(t_0 + K_{3,3}\right)\right)$

APPENDIX B

ONE-DIMENSIONAL SOLIDIFICATION

Consider a semi-infinite medium, initially in a liquid state and at a uniform temperature, u_∞, above the equilibrium melting temperature, u_m. The left boundary ($x = 0$) is suddenly brought to a temperature u_0 ($= 0$), below the equilibrium melting temperature and solidification begins [17].

Conduction of thermal energy in the solid and the liquid is governed by the one-dimensional heat equation:

$$\frac{\partial u_i}{\partial t} = \alpha_i \frac{\partial^2 u_i}{\partial x^2} \tag{B.1}$$

where the subscript i denotes either the solid phase, s, or the liquid phase ℓ. A constant temperature is applied at the left boundary:

$$u|_{x=0} = 0, \tag{B.2}$$

and the solid-liquid interface is assumed to be a the equilibrium melting temperature:

$$u|_{x=y(t)} = u_m, \tag{B.3}$$

where $y(t)$ is the position of the solid front. A heat balance is also applied a the solid-liquid interface:

$$k_s \left.\frac{\partial u}{\partial x}\right|_{x=y(t)} - k_\ell \left.\frac{\partial u}{\partial x}\right|_{x=y(t)} = L\rho \frac{dy(t)}{dt} \tag{B.4}$$

It can be shown that the error function is a solution to Equation B.1:

$$u_s = A\mathrm{erf}\left[\frac{x}{2(\alpha_s t)^{1/2}}\right] \tag{B.5}$$

$$u_\ell = B + C\mathrm{erfc}\left[\frac{x}{2(\alpha_\ell t)^{1/2}}\right] \tag{B.6}$$

Applying the equilibrium solidification condition it is found that

$$A \mathrm{erf}\left[\frac{y(t)}{2(\alpha_s t)^{1/2}}\right] = u_m \tag{B.7}$$

This condition must be met for all time, and therefore, the position of the solid front must be proportional to the square root of time. The position of the solid front can therefore be expressed as

$$y(t) = 2\lambda(\alpha_s t)^{1/2} \tag{B.8}$$

Knowing the form of the equation for the solid front position, the value of the coefficients may be determined:

$$A = \frac{u_m}{\mathrm{erf}[\lambda]} \tag{B.9}$$

$$B = u_\infty \tag{B.10}$$

$$C = -\frac{u_\infty - u_m}{\mathrm{erf}\left[\lambda(\alpha_s/\alpha_\ell)^{1/2}\right]} \tag{B.11}$$

Imposing the heat balance at the solid front, the constant, λ, may be defined through a transcendental equation:

$$\frac{\mathrm{Ste}_s}{e^{\lambda^2}\mathrm{erf}[\lambda]} - \frac{\mathrm{Ste}_\ell}{e^{\lambda^2\alpha_s/\alpha_\ell}\mathrm{erfc}\left[\lambda(\alpha_s/\alpha_\ell)^{1/2}\right]} = \pi^{1/2}\lambda \tag{B.12}$$

where Ste_s and Ste_ℓ are the solid and liquid Stefan numbers, respectively:

$$\mathrm{Ste}_s = \frac{c_{p,s}u_m}{\Delta H}, \quad \mathrm{Ste}_\ell = \frac{c_{p,\ell}(u_\infty - u_m)}{\Delta H} \tag{B.13}$$

For the special case when the material is initially liquid at the equilibrium melting temperature

$$\lambda e^{\lambda^2}\mathrm{erf}[\lambda] = \mathrm{Ste}_s \tag{B.14}$$

APPENDIX C

ONE-DIMENSIONAL SOLIDIFICATION WITH CONTACT RESISTANCE

Consider a semi-infinite medium, initially in a liquid state and at the equilibrium melting temperature, with a convective heat transfer condition applied at the left boundary ($x = 0$). Conduction of thermal energy in the solid will be governed by the heat equation:

$$\frac{\partial T}{\partial t} = \alpha \frac{\partial^2 T}{\partial x^2}, \tag{C.1}$$

where T is the temperature , and α is the thermal diffusivity in the solid. A convective heat transfer condition is applied at the left boundary:

$$k \left. \frac{\partial T}{\partial x} \right|_{x=0} = h \left(T|_{x=0} - T_0 \right), \tag{C.2}$$

where k is the thermal conductivity in the solid and T_0 is the substrate temperature. Furthermore, a heat balance is applied at the right boundary:

$$k \left. \frac{\partial T}{\partial x} \right|_{x=S} = \Delta H \rho \frac{dS}{dt}, \tag{C.3}$$

where ΔH is the latent heat of fusion, ρ is the density of the solid and S is the solid front position. Solidification is assumed to be an equilibrium process; consequently the temperature at the solid front position is set to the equilibrium melting temperature,

$$T|_{x=S} = T_m, \tag{C.4}$$

where T_m is the equilibrium melting temperature.

Chosing an appropriate length scale ($x^* = L$), and using a time scale ($t^* =$

$\rho c_p L/h)$, Equation B.1 may be cast in dimensionless form giving

$$\frac{\partial \Theta}{\partial \tau} = \frac{1}{Bi}\frac{\partial^2 \Theta}{\partial \chi^2}, \tag{C.5}$$

where Θ is the dimensionless temperature, τ is the dimensionless time, and χ is the dimensionless position:

$$\Theta = \frac{T - T_0}{T_m - T_0}, \ \tau = \frac{t}{t^*}, \text{ and } \chi = \frac{x}{x^*}. \tag{C.6}$$

Bi is the Biot number and is given by

$$\text{Bi} = \frac{hL}{k}. \tag{C.7}$$

Using the length and time scales from above, the convective heat transfer condition at the left boundary becomes

$$\left.\frac{\partial \Theta}{\partial \chi}\right|_{\chi=0} = \text{Bi } \Theta|_{\chi=0}, \tag{C.8}$$

and the heat balance at the solid front becomes

$$\left.\frac{\partial \Theta}{\partial \chi}\right|_{chi=\Lambda} = \frac{\text{Bi}}{\text{Ste}}\frac{d\Lambda}{d\tau}, \tag{C.9}$$

where Λ is the dimensionless solid front position and Ste is the Stefan number,

$$\text{Ste} = \frac{\Delta H}{c_p\,(T_m - T_0)}. \tag{C.10}$$

A solution is desired for this problem; however, because of the non-linearity introduced due to the moving boundary, the solution may no be found through separation of variables. Furthermore, the convective heat flux boundary condition can not be satisfied with the error function solution to the heat equation. However, it may be shown that the double power series,

$$\begin{aligned}\Theta = & \sum_{i=0}^{\infty} a_i \sum_{j=0}^{i} \frac{(2i)!}{(2j)!\,(i-j)!} \left(\frac{\tau}{\mathrm{Bi}}\right)^{i-j} \chi^{2j} \\ & + \sum_{i=0}^{\infty} b_i \sum_{j=0}^{i} \frac{(2i+1)!}{(2j+1)!\,(i-j)!} \left(\frac{\tau}{\mathrm{Bi}}\right)^{i-j} \chi^{2j+1},\end{aligned} \tag{C.11}$$

is a solution to the heat equation, and the position of the solid front as a function of time may be expressed and a power series,

$$\Lambda = \sum_{n=0}^{\infty} c_n t^n. \tag{C.12}$$

The coefficients, a_i, b_i and c_i, may be determined by applying Equation C.11 to the boundary and initial conditions. First, the condition that the medium is initially liquid is used. From this condition it is found that $c_0 = 0$. Next, the convective heat flux condition at the left boundary is use to determine b_i is terms of a_i,

$$b_i = \frac{\mathrm{Bi}}{2i+1} a_i. \tag{C.13}$$

Using Equation C.11, a general expression may be found for the coefficients a_i,

$$\begin{aligned}a_m = & \frac{m!}{(2m)!} \mathrm{Bi}^m \left[\sum_{i=0}^{m-1} a_i \sum_{j=0}^{i} \frac{(2i)!}{(2j)!\,(i-j)!} \mathrm{Bi}^{j-i} \Omega\left(\Lambda, m-i+j, 2j\right) \right. \\ & \left. + \sum_{i=0}^{m-1} b_i \sum_{j=0}^{i} \frac{(2i+1)!}{(2j+1)!\,(i-j)} \mathrm{Bi}^{j-i} \Omega\left(\Lambda, m-i+j, 2j+1\right) \right],\end{aligned} \tag{C.14}$$

where

$$\Omega\left(\Lambda, m, n\right) = \sum_{k_1=0}^{m} \sum_{k_2=0}^{m-k_1} \cdots \sum_{k_n-1}^{m-(k_1+k_2+\ldots+k_{n-2})} c_{k_1} c_{k_2} \ldots c_{k_{n-1}} c_{m-(k_1+k_2+\ldots+k_{n-1})}. \tag{C.15}$$

The function $\Omega\left(\Lambda, m, n\right)$ may be taken as the coefficient of the τ^m term of Λ raised to the power n. For $n = 0$, a value of unity will be given if $m = 0$, and a value of zero if $m \neq 0$. Using the heat balance at the solid-liquid interface, a general expression may be found for the coefficients c_i,

$$c_m = \frac{\text{Ste}}{m\text{Bi}} \left[\sum_{i=1}^{m-1} a_i \sum_{j=1}^{i} \frac{(2i)!}{(2j-1)!\,(i-j)!} \text{Bi}^{j-i} \Omega\left(\Lambda, m-1-i+j, 2j-1\right) + \sum_{i=0}^{m-1} b_i \sum_{j=0}^{i} \frac{(2i+1)!}{(2j)!\,(i-j)!} \text{Bi}^{j-i} \Omega\left(\Lambda, m-1-i+j, 2j\right) \right] \tag{C.16}$$

Coefficient	value
c_0	0
c_1	Ste
c_2	$-\dfrac{\text{BiSte}^2\left(1+\text{Ste}\right)}{2}$
c_3	$\dfrac{\text{Bi}^2\text{Ste}^3\left(3+8\text{Ste}+5\text{Ste}^2\right)}{6}$
c_4	$-\dfrac{\text{Bi}^3\text{Ste}^4\left(105+421\text{Ste}+573\text{Ste}^2+255\text{Ste}^3\right)}{120}$
c_5	$\dfrac{\text{Bi}^4\text{Ste}^5\left(1215+6384\text{Ste}+13056\text{Ste}^2+12030\text{Ste}^3+4135\text{Ste}^4\right)}{600}$

Table C.1: Coefficients for solid front position power series.

Approximations to the solid front position are ploted using one to five terms of the power series (Figure C.1). The power series is poorly behaved for high Biot numbers. However, for low Biot numbers, typically found in spray deposition processes, the solid front advances with a nearly linear relation to time (Figure C.2).

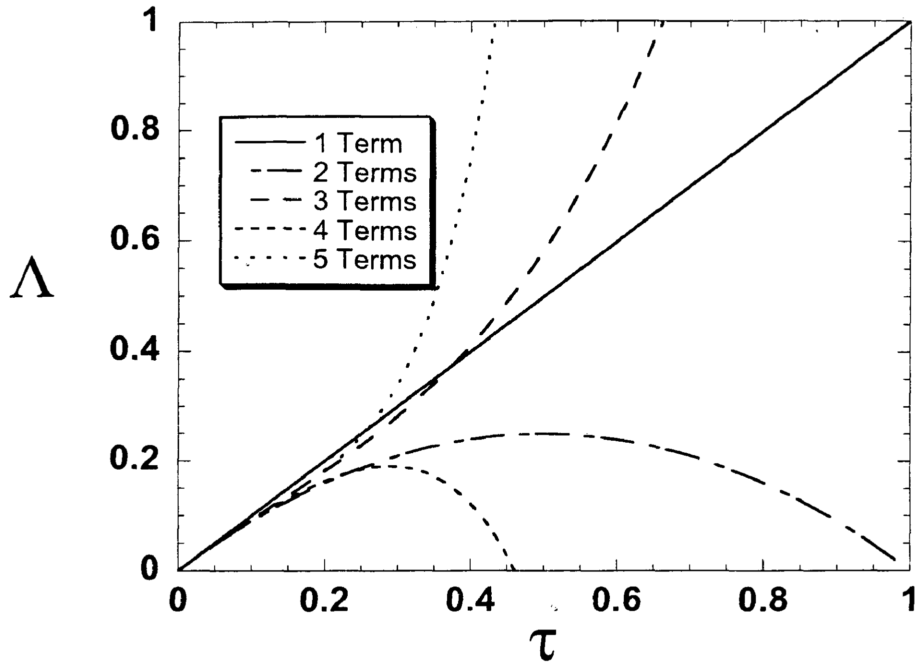

Figure C.1: Solid front position for Bi = 1, Ste = 1.

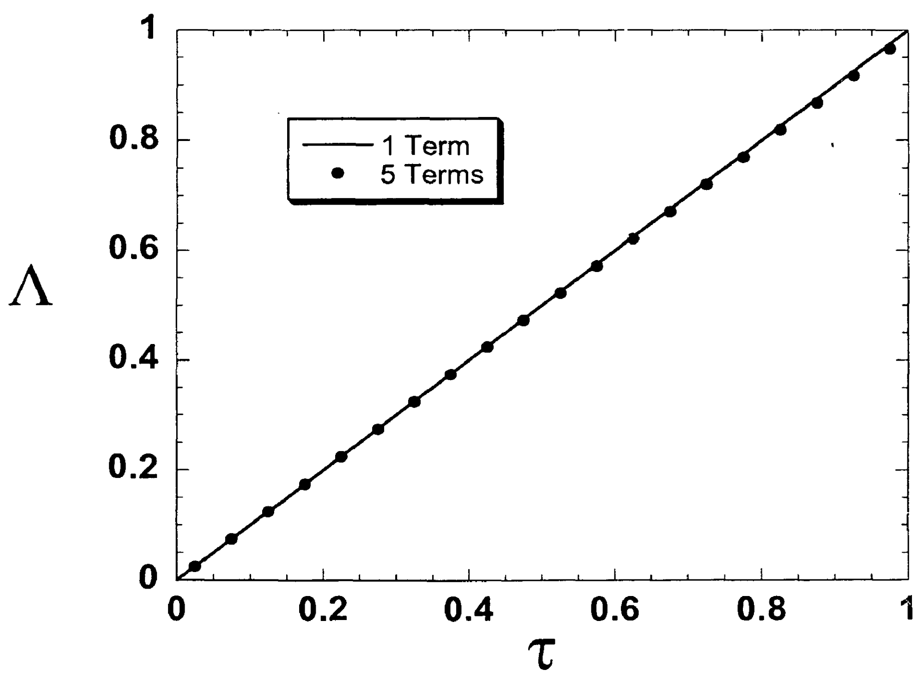

Figure C.2: Solid front position for Bi = .01, Ste = 1.